


Atmos. Meas. Tech., 6, 2803–2823, 2013  
www.atmos-meas-tech.net/6/2803/2013/  
doi:10.5194/amt-6-2803-2013  
© Author(s) 2013. CC Attribution 3.0 License.



Atmospheric  
Measurement  
Techniques  
Open Access  


# Global monitoring of terrestrial chlorophyll fluorescence from moderate-spectral-resolution near-infrared satellite measurements: methodology, simulations, and application to GOME-2

J. Joiner<sup>1</sup>, L. Guanter<sup>2</sup>, R. Lindstrot<sup>2</sup>, M. Voigt<sup>2</sup>, A. P. Vasilkov<sup>3</sup>, E. M. Middleton<sup>1</sup>, K. F. Huemmrich<sup>4</sup>, Y. Yoshida<sup>3</sup>, and C. Frankenberg<sup>5</sup>

<sup>1</sup>NASA Goddard Space Flight Center, Greenbelt, MD, USA

<sup>2</sup>Free University of Berlin, Berlin, Germany

<sup>3</sup>Science Systems and Applications, Inc., Lanham, MD, USA

<sup>4</sup>University of Maryland, Baltimore County, Joint Center for Environmental Technology (UMBC-JCET), Baltimore, MD, USA

<sup>5</sup>Jet Propulsion Laboratory, California Institute of Technology, Pasadena, CA, USA

Correspondence to: J. Joiner ([joanna.joiner@nasa.gov](mailto:joanna.joiner@nasa.gov))

Received: 23 March 2013 – Published in Atmos. Meas. Tech. Discuss.: 22 April 2013

Revised: 15 August 2013 – Accepted: 4 September 2013 – Published: 25 October 2013

**Abstract.** Globally mapped terrestrial chlorophyll fluorescence retrievals are of high interest because they can provide information on the functional status of vegetation including light-use efficiency and global primary productivity that can be used for global carbon cycle modeling and agricultural applications. Previous satellite retrievals of fluorescence have relied solely upon the filling-in of solar Fraunhofer lines that are not significantly affected by atmospheric absorption. Although these measurements provide near-global coverage on a monthly basis, they suffer from relatively low precision and sparse spatial sampling. Here, we describe a new methodology to retrieve global far-red fluorescence information; we use hyperspectral data with a simplified radiative transfer model to disentangle the spectral signatures of three basic components: atmospheric absorption, surface reflectance, and fluorescence radiance. An empirically based principal component analysis approach is employed, primarily using cloudy data over ocean, to model and solve for the atmospheric absorption. Through detailed simulations, we demonstrate the feasibility of the approach and show that moderate-spectral-resolution measurements with a relatively high signal-to-noise ratio can be used to retrieve far-red fluorescence information with good precision and accuracy. The method is then applied to data from the Global Ozone Monitoring Instrument 2 (GOME-2). The GOME-2 fluores-

cence retrievals display similar spatial structure as compared with those from a simpler technique applied to the Greenhouse gases Observing SATellite (GOSAT). GOME-2 enables global mapping of far-red fluorescence with higher precision over smaller spatial and temporal scales than is possible with GOSAT. Near-global coverage is provided within a few days. We are able to show clearly for the first time physically plausible variations in fluorescence over the course of a single month at a spatial resolution of  $0.5^\circ \times 0.5^\circ$ . We also show some significant differences between fluorescence and coincident normalized difference vegetation indices (NDVI) retrievals.

## 1 Introduction

Vegetation releases unused absorbed photosynthetically active radiation primarily as heat with a small amount re-emitted as fluorescence. Measurements of terrestrial chlorophyll fluorescence are directly related to photosynthetic function, and are potentially useful for forest and agricultural applications as well as assessment of the terrestrial carbon budget by providing more accurate estimates of gross primary productivity (GPP) (e.g., Lichtenthaler, 1987; Saito et al., 1998; Corp et al., 2003, 2006; Campbell et al.,

2008; Damm et al., 2010; Joiner et al., 2011, 2012; Frankenberg et al., 2011b; Guanter et al., 2012). Studies show that in high light conditions, such as in the late morning and early afternoon, when many satellite measurements are made and when plants are under stress, fluorescence is correlated to the amount of absorbed photosynthetically active radiation (APAR) and the efficiency of the plants to utilize this light to drive photosynthesis (light-use efficiency or LUE) (e.g., Flexas et al., 2002; Louis et al., 2005; Meroni et al., 2008; Amoros-Lopez et al., 2008; van der Tol et al., 2009; Zarco-Tejada et al., 2009, 2013; Daumard et al., 2010).

Fluorescence information is also complementary to reflectance-based spectral vegetation indices (Meroni and Colombo, 2006; Middleton et al., 2008, 2009; Rascher et al., 2009; Meroni et al., 2008; Daumard et al., 2010; Guanter et al., 2007, 2012; Zarco-Tejada et al., 2009, 2013; Joiner et al., 2011, 2012; Frankenberg et al., 2011b). For example, popular greenness-based indices such as the normalized difference and enhanced vegetation indices (NDVI and EVI, respectively) are linked to chlorophyll content and are related to potential photosynthesis, whereas fluorescence should be an indicator of actual photosynthesis. The photochemical reflectance index (PRI) is sensitive to the de-epoxidation state of pigments within xanthophyll cycle, a protection mechanism that evolved in parallel to fluorescence to dissipate excess energy (Gamon et al., 1992).

Knowledge of global chlorophyll fluorescence emissions is also important for retrievals of trace-gas concentrations including CO<sub>2</sub> that require very high accuracy and precision. The emission occurs within the O<sub>2</sub> A-band that is used to estimate photon path lengths for these measurements. If not properly accounted for, fluorescence emission may produce significant errors in these retrievals (Frankenberg et al., 2012). The effect of fluorescence on an aerosol plume height retrieval from the O<sub>2</sub> A-band has also been investigated using a linear error analysis with simulated data (Sanders and de Haan, 2013).

One means of measuring the small fluorescence signal from passive remote sensing instrumentation is to make use of dark features in the Earth's reflected spectrum, either from telluric absorption or deep solar Fraunhofer lines. For example, ground-, aircraft-, and space-based approaches have utilized filling-in of the dark and spectrally wide O<sub>2</sub> A-band (~760 nm) and O<sub>2</sub> B-band (~690 nm) atmospheric absorption features to detect the weak fluorescence signal (see, e.g., Guanter et al., 2007; Meroni et al., 2009, 2010). The spectral location of these oxygen absorption features as well as other absorption bands and solar Fraunhofer lines are shown in Fig. 1 along with the broadband red and far-red fluorescence emission features that peak near 685 and 740 nm, respectively.

Deep solar Fraunhofer lines have also been used to detect fluorescence from vegetation following the early work of, e.g., Plascyk and Gabriel (1975). Joiner et al. (2011, 2012), Frankenberg et al. (2011b), and Guanter et al. (2012)

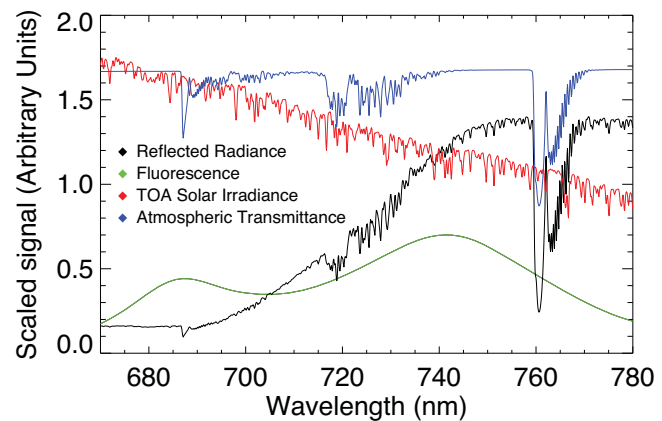


**Fig. 1.** Simulated solar-induced terrestrial fluorescence, typical simulated atmospheric transmittance and reflectance, and solar irradiance as a function of wavelength computed for an instrument with FWHM = 0.3 nm. The fluorescence shows red and far-red chlorophyll emission features with peaks near 685 and 740 nm, respectively. Oxygen A and B absorption bands are located near 687 and 760 nm, respectively, while water vapor absorption is shown over a broad spectral range between about 690 and 740 nm. The solar irradiance shows weak solar Fraunhofer line structure at this spectral resolution.

used near-infrared (NIR) solar Fraunhofer lines, which are filled in by vegetation fluorescence, to globally map terrestrial fluorescence with the high-spectral-resolution interferometer aboard the Japanese Greenhouse gases Observing SATellite (GOSAT). Joiner et al. (2012) strongly suggested that fluorescence may also be measurable from space with lower-spectral-resolution instrumentation as compared with the GOSAT interferometer or similar instruments. They focused on filling-in of the 866 nm Ca II solar Fraunhofer line as measured with the SCanning Imaging Absorption spectroMeter for Atmospheric CHartographY (SCIAMACHY) satellite instrument. This filling-in appears to be produced by fluorescence from chlorophyll as supported by Gamon and Berry (2012). The SCIAMACHY spectral resolution at this wavelength is about 0.5 nm.

While the current satellite results show promise for use in estimation of GPP, the GOSAT measurements have fairly low spatial sampling and relatively low single-observation precision (Joiner et al., 2011; Frankenberg et al., 2011a; Guanter et al., 2012). The SCIAMACHY results have higher sampling frequency, but the very low signal levels spectrally far from the far-red fluorescence peak also result in low precision for single observations (Joiner et al., 2012). To produce global maps with high enough fidelity for comparisons with other measurements and models, GOSAT and SCIAMACHY fluorescence retrievals must be averaged spatially and/or temporally. In doing so for GOSAT, there can be a substantial sampling or representativeness error introduced by the averaging of sparse observations within a relatively large grid box.

Other approaches for satellite fluorescence retrievals have aimed at utilization of the strong atmospheric oxygen bands (A and B bands) that absorb at wavelengths where chlorophyll fluorescence is emitted. For example, approaches to separate fluorescence features from those of reflectance for space-based measurements have been developed in which atmospheric absorption is assumed to be perfectly modeled (e.g., Mazzoni et al., 2008, 2010, 2012). More complex algorithms have been proposed and tested on simulated data in which the parameters affecting O<sub>2</sub> absorption are retrieved and accounted for using a radiative transfer model (Guanter et al., 2010). Low-spectral-resolution O<sub>2</sub> A-band satellite measurements from the MEdium Resolution Imaging Spectrometer (MERIS) aboard Envisat have also been used to retrieve information about fluorescence (Guanter et al., 2007). Thus far, these satellite measurements are spatially and temporally limited and require an on-ground nearby nonfluorescing reference target for normalization.

Here, we develop new methodology to retrieve the far-red chlorophyll fluorescence using space-based hyperspectral measurements in and around the O<sub>2</sub> A-band. Instead of exclusively using the filling-in of solar Fraunhofer lines as in the previous works with GOSAT and SCIAMACHY, we demonstrate that fluorescence can be retrieved by exploiting the different spectral structure produced by the far-red chlorophyll fluorescence feature (including both solar and telluric line filling), atmospheric absorption, and surface reflectance.

Our methodology is similar to approaches developed for ground-based instrumentation (Guanter et al., 2013) in that radiative transfer in atmospheric absorption bands is approximated statistically using a principal component analysis (PCA) (or singular value decomposition, SVD). SVD approaches have also been applied to satellite fluorescence retrievals using wavelengths not affected by atmospheric absorption (Guanter et al., 2012). In this work, we expand the use of PCA to include the geometry of a space-based instrument for wavelengths where significant atmospheric absorption takes place. This scenario is more complex than for ground-based measurements. Fluorescence emission can be significantly absorbed in the atmosphere. Because this absorption is different in magnitude from that of reflected sunlight, the scenario for a satellite retrieval is more difficult as compared with that for a ground-based instrument. While our approach does not require a nearby nonfluorescing target as in other techniques, a representative sample of observations over nonfluorescing scenes is needed in order to generate a comprehensive set of PCs. For this purpose, we use cloudy observations over ocean covering a large range of latitudes on a daily basis.

We conduct simulations to demonstrate the applicability of our approach to current and proposed satellite instruments. We then apply our technique to data from the Global Ozone Monitoring Instrument 2 (GOME-2). The primary function of GOME-2 is to make measurements of atmospheric trace

gases. While not optimal for fluorescence measurements owing to its relatively large ground footprint and moderate spectral resolution, its high sampling and signal-to-noise ratio enable state-of-the-art fluorescence retrievals in the far-red chlorophyll emission feature. Near-global coverage is provided within a few days from GOME-2 measurements with a high signal-to-noise ratio. Accurate and frequent measurements from GOME-2 will lead to a fluorescence data set with unprecedented temporal and spatial resolution; this in turn should enable detailed studies including more direct comparisons with flux tower measurements.

## 2 GOME-2 satellite data

In this work, we use data from GOME-2. GOME-2 is an operational nadir-viewing UV/visible cross-track scanning spectrometer (Munro et al., 2006). It flies as part of the European Meteorological Satellite (EUMETSAT) Polar System (EPS) MetOp mission series. GOME-2 measures the Earth's backscattered radiance and the extraterrestrial solar irradiance at wavelengths between 240 and 790 nm in four detector channels. Here, we use level 1B data from revision R2 in channel 4 that cover wavelengths 590–790 nm with a spectral resolution of approximately 0.5 nm (Callies et al., 2000) and a relatively high SNR (> 1000).

The nadir Earth footprint size is 40 km × 80 km, and the nominal swath width is 1920 km. A single GOME-2 instrument provides global coverage of the Earth's surface in about 1.5 days. The first flight of GOME-2 is on MetOp-A, launched 19 October 2006 into a polar orbit with an equator crossing time of 09:30 LT. The second flight, launched 17 September 2012 on MetOp-B, is also in a morning orbit but 180° out of phase with the first flight model. As such, one or the other instrument is always making measurements on the sunlit part of the Earth, and near-global daily coverage is achievable.

## 3 Simulated radiances and irradiances

Because our approach relies on an empirical rather than a physical approach for deriving atmospheric absorption, it is difficult to quantify forward model errors. To accurately quantify retrieval errors, we conduct detailed simulations using combined atmospheric and vegetation models over a wide range of conditions. We also use simulated data to assess the impact of instrument specifications including the signal-to-noise ratio (SNR) and spectral resolution on fluorescence retrievals. Finally, we test different retrieval scenarios, such as various spectral fitting windows and numbers of retrieved parameters, using the simulated radiances.

We simulate top-of-the-atmosphere (TOA) sun-normalized radiances using the matrix operator model (MOMO) radiative transfer model (Fell and Fischer, 2001; Preusker and Lindstrot, 2009). The radiance calculations

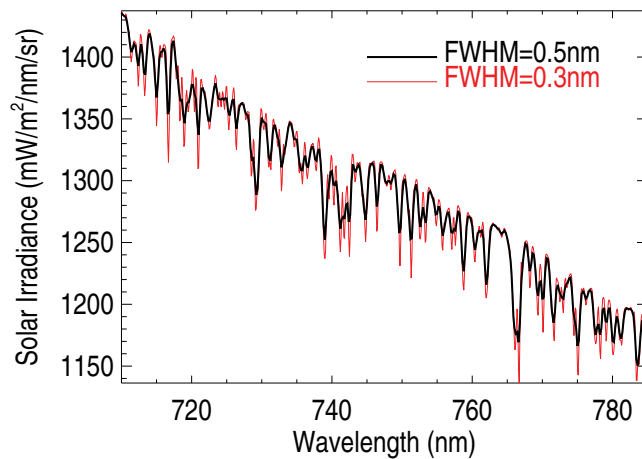


**Fig. 2.** Simulated solar spectra based on Chance and Kurucz (2010) for different instrumentation showing Fraunhofer line structure (FWHM = 0.5 nm is for a GOME-2-like instrument).

utilize absorption line strengths and widths from the high-resolution atmospheric radiance and transmittance model code (HITRAN) 2008 data set (Rothman et al., 2009). The radiances are computed monochromatically and are sampled at 0.005 nm. They are then multiplied by a solar spectrum sampled in the same way and finally convolved with various instrument line shape functions.

We use solar data originally sampled at 0.001 nm from kurucz.harvard.edu/sun/irradiance2005/irradthu.dat, similar to Chance and Kurucz (2010) but more highly sampled. Figure 2 shows simulated solar spectra generated for different instrument specifications including a spectral resolution similar to GOME-2 (i.e., full width at half maximum (FWHM) of 0.5 nm sampled at 0.2 nm) and a smaller FWHM of 0.3 nm sampled at 0.1 nm. Significant solar Fraunhofer line structure can be seen throughout the spectrum with deeper structures at the higher spectral resolution.

Note that we do not simulate the effects of rotational Raman scattering (RRS) or O<sub>2</sub> A-band dayglow emissions. RRS effects are generally small, though not negligible, at the wavelengths of interest (Vasilkov et al., 2013). The effects of O<sub>2</sub> A-band dayglow emissions in the upper atmosphere are expected to be small (Guanter et al., 2010). Directional effects of the vegetation reflectance and fluorescence are also not simulated.

Radiances are computed for two view zenith angles (VZA = 0 and 16°), four solar zenith angles (SZA = 15°, 30°, 45°, 70°), two atmospheric temperature profiles (middle latitude summer and winter), four surface pressures (955, 980, 1005, and 1030 hPa), four values of total column water vapor (0.5, 1.5, 2.5, and 4.0 cm), five aerosol optical thicknesses at 550 nm (0.05, 0.12, 0.2, 0.3, and 0.4), and three aerosol plume heights (700–900, 600–800, and 500–700 hPa) with a continental aerosol model. Two separate data sets are created, one without fluorescence intended for prin-

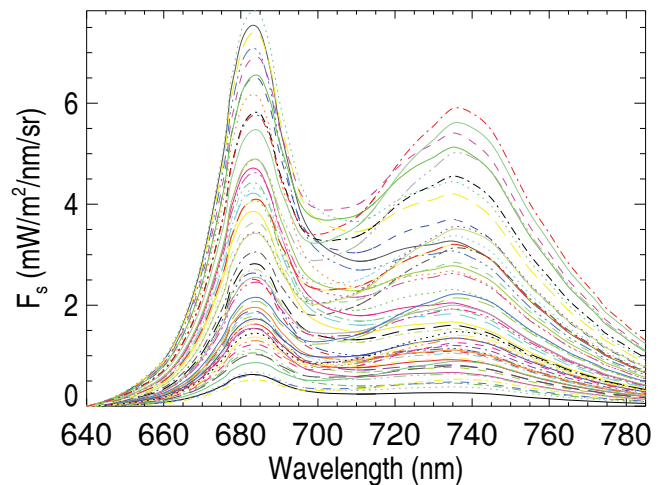


**Fig. 3.** Canopy-level spectral fluorescence as specified for the range of conditions in the simulated data set.

cipal component analyses (henceforth referred to as “training”), and one containing fluorescence intended to examine retrieval performance with the simulated radiances (referred to as “testing”). The training data set uses a spectral library of 10 different surface reflectance spectra corresponding to soil and snow. This provides a total of 38 400 samples in the training data set.

The testing data set contains surface reflectance and fluorescence emission spectra generated with the FluorSAIL and FluorMODleaf codes (Jacquemoud et al., 2009; Pedrós et al., 2010; Miller et al., 2005). A given input leaf-level fluorescence spectrum has been scaled by multiplicative factors. Different values of chlorophyll content (from 5 to 40  $\mu\text{g cm}^{-2}$ ) and leaf area index (from 0.5 to 4) have been used for the propagation of the resulting leaf-level fluorescence spectra to the canopy level. There are 60 distinct top-of-canopy fluorescence spectra from these combinations as shown in Fig. 3. Top-of-canopy reflectance spectra are consistently generated by the leaf and canopy codes for the same combinations of chlorophyll content and leaf area index. Other parameters in the models were set to default values as in Guanter et al. (2010). This gives a total of 230 400 different samples in the testing data set.

## 4 Retrieval methodology

### 4.1 General approach

The total reflectance  $\rho_{\text{tot}}$ , as a function of wavelength  $\lambda$ , measured by a satellite instrument in the NIR spectral region, can be approximated using a Lambertian model with emission from fluorescence, i.e.,

$$\rho_{\text{tot}}(\lambda) = \rho_0(\lambda) + \frac{\rho_s(\lambda)\mathcal{T}(\lambda)\bar{\mathcal{T}}(\lambda)}{1 - \rho_s(\lambda)\bar{\rho}(\lambda)} + \frac{\pi F_s(\lambda)\bar{\mathcal{T}}(\lambda)}{[1 - \rho_s(\lambda)\bar{\rho}(\lambda)]E(\lambda)\cos(\theta_0)}, \quad (1)$$

where  $\rho_s(\lambda)$  is the surface reflectance,  $\rho_0$  is the reflectance contribution in the absence of surface effects,  $\mathcal{T}$  is the total irradiance transmittance (including direct and diffuse components),  $\overline{\mathcal{T}}$  is the spherical transmittance from the surface to TOA,  $\overline{\rho}$  is the spherical reflectance of the atmosphere back to the surface,  $\theta_0$  is the solar zenith angle (SZA),  $E(\lambda)$  is the observed extraterrestrial solar irradiance, and  $F_s$  is the radiance emission from fluorescence at the surface.

The basic idea behind our approach is to separate the spectral features related to three basic components: atmospheric absorption ( $\mathcal{T}$  and  $\overline{\mathcal{T}}$ ), surface reflectivity ( $\rho_s$ ), and fluorescence radiance ( $F_s$ ). Assuming that the effects of atmospheric scattering are small (i.e.,  $\rho_0 \simeq 0$  and  $\rho_s \overline{\rho} \ll 1$ ), we may rewrite Eq. (1) as

$$\rho_{\text{tot}}(\lambda) = \rho_s(\lambda)\mathcal{T}(\lambda)\overline{\mathcal{T}}(\lambda) + \frac{\pi F_s(\lambda)\overline{\mathcal{T}}(\lambda)}{E(\lambda)\cos(\theta_0)}, \quad (2)$$

where  $\mathcal{T}(\lambda)$  and  $\overline{\mathcal{T}}(\lambda)$  now include atmospheric molecular absorption only. We now combine  $\mathcal{T}$  and  $\overline{\mathcal{T}}$  into a single parameter,  $\mathcal{T}_2(\lambda) = \mathcal{T}(\lambda)\overline{\mathcal{T}}(\lambda)$ , that represents the sun-to-satellite (two-way) atmospheric transmittance. Using

$$\begin{aligned} \mathcal{T}_2(\lambda) &= \exp[-\mathcal{A}_2(\lambda)] \\ &= \exp[-\mathcal{A}_v(\lambda)\{\sec(\theta) + \sec(\theta_0)\}], \end{aligned} \quad (3)$$

where  $\theta$  is the satellite view zenith angle (VZA), and  $\mathcal{A}_2$  and  $\mathcal{A}_v$  represent the two-way and vertical absorptances, respectively, and the upwards absorptance,  $\overline{\mathcal{A}}$ , as

$$\begin{aligned} \overline{\mathcal{A}}(\lambda) &= \mathcal{A}_v(\lambda)\sec(\theta) \\ &= \mathcal{A}_2(\lambda)\frac{\sec(\theta)}{\sec(\theta) + \sec(\theta_0)}, \end{aligned} \quad (4)$$

then

$$\overline{\mathcal{T}}(\lambda) = \exp\left(\ln[\mathcal{T}_2(\lambda)]\frac{\sec(\theta)}{\sec(\theta) + \sec(\theta_0)}\right). \quad (5)$$

Note that the above equations are strictly valid only for monochromatic radiation. Also note that  $\rho_0$ ,  $\overline{\rho}$ ,  $\overline{\mathcal{T}}$ , and  $\mathcal{T}$ , in the presence of atmospheric scattering and in the absence of atmospheric molecular absorption, are a spectrally smooth function of wavelength. Therefore, when atmospheric scattering is present,  $\rho_s(\lambda)$  and  $F_s(\lambda)$  in Eq. (2) can be thought of as effective TOA spectral components of surface reflectance and fluorescence that have been modified by spectrally smooth atmospheric scattering; the spectral structure of  $\rho_0$  can be incorporated into the components of the first term of Eq. (2).

To solve for  $\rho_s$ ,  $F_s$ , and  $\mathcal{T}_2$ , we assume that each has a distinct spectral structure. We represent the fluorescence far-red emission,  $F_s(\lambda)$ , as a Gaussian function of  $\lambda$  centered at 736.8 nm with  $\sigma = 21.2$  nm, similar to Subhash and Mohanan (1997) and Zarco-Tejada et al. (2000). We further assume that  $\rho_s(\lambda)$ , within our limited spectral fitting window, is spectrally

smooth, and model it as a low-order polynomial in  $\lambda$ . Alternative parameterizations for fluorescence and reflectance have been explored (e.g., Mazzoni et al., 2010, 2012). Previous works suggest that small errors in the prescribed shape of the fluorescence emission have little impact on the estimated peak fluorescence value (Daumard et al., 2010; Fournier et al., 2012; Guanter et al., 2013). We estimate the spectral structure of  $\mathcal{A}_2$  (or  $\mathcal{T}_2$ ) using principal components (PCs) as described below.

In principle, our approach may be applied to the entire fluorescence emission band shown in Fig. 1 containing both the red and far-red features. Alternatively, different fitting windows could be used to estimate fluorescence within smaller wavelength ranges. As a starting point to demonstrate our approach, we focus on retrievals of the far-red fluorescence.

## 4.2 Generation of atmospheric PCs

Radiative transfer in the O<sub>2</sub> A-band is complex because the shape of the absorption features depends nonlinearly upon the surface pressure and albedo as well as the vertical structure of atmospheric temperature and cloud/aerosol particles (e.g., Preusker and Lindstrot, 2009). Absorption by water vapor in the 710–745 nm spectral region also depends upon these parameters and is similarly complex; though less affected by saturated lines, the profile is of course more variable. Retrieval algorithms have been developed to retrieve some or all of these parameters using O<sub>2</sub> A-band radiances (e.g., Guanter et al., 2007; O’Dell et al., 2012). Other factors such as filling-in from rotational Raman scattering are typically not accounted for owing to a high degree of complexity resulting from interactions with Mie scattering and dependences on other parameters (Vasilkov et al., 2013). Neglect of these effects may produce errors in such algorithms. Instrumental effects such as nonlinearity also challenge physically based approaches used to estimate O<sub>2</sub> A-band absorption.

Instead of using radiative transfer calculations, we have developed an empirically based alternative for estimation of  $\mathcal{A}_2$  or  $\mathcal{T}_2(\lambda)$ ; we represent  $\mathcal{A}_2(\lambda)$  as a linear combination of principal components (PCs)  $\phi_i(\lambda)$  that can be estimated using simulated or real satellite data, i.e.,

$$\mathcal{A}_2(\lambda) = \sum_{i=1}^n a_i \phi_i(\lambda), \quad (6)$$

where  $a_i$  are the coefficients of the PCs. Instead of using laboratory-measured absorption cross sections, as is typical in the differential optical absorption spectroscopy (DOAS) approach, we use atmospheric spectra, simulated or measured, to derive the spectral components of absorption.

As in the DOAS approach, our method implicitly assumes that the Beer–Lambert law of weak linear absorption applies, although the PCs may be able to incorporate some features of nonlinear absorption. Because this law does not strictly apply to the O<sub>2</sub> A-band, where individual lines may become

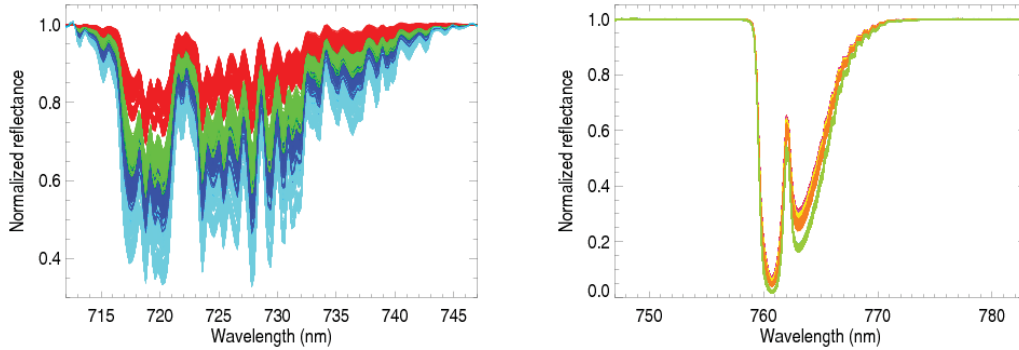


**Fig. 4.** Transmittances derived from the training data set with FWHM = 0.5 nm. Colors in the left panel correspond to values of total column water vapor (light blue, dark blue, green, and red correspond to 4.0, 2.5, 1.5, and 0.5 cm, respectively) for various combinations of solar and viewing zenith angles; colors on right-hand panel showing O<sub>2</sub> A-band absorption correspond to different combinations of solar and viewing zenith angles.

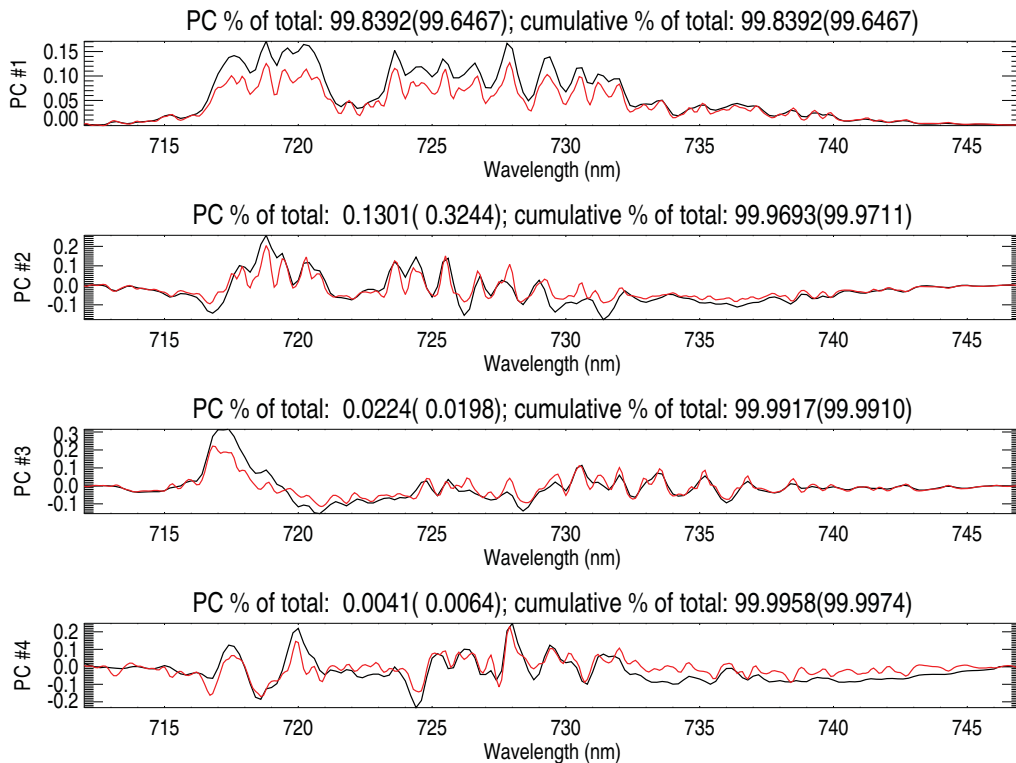


**Fig. 5.** Leading principal components (PCs) of simulated reflectance spectra for the short-wavelength fitting window for a GOME-like instrument with FWHM = 0.5 nm (black) and a higher-spectral-resolution instrument with FWHM = 0.3 nm (red); numbers in the top title are the variance explained in terms of percent of the total and cumulative percent of the total with numbers for FWHM = 0.3 nm in parentheses.

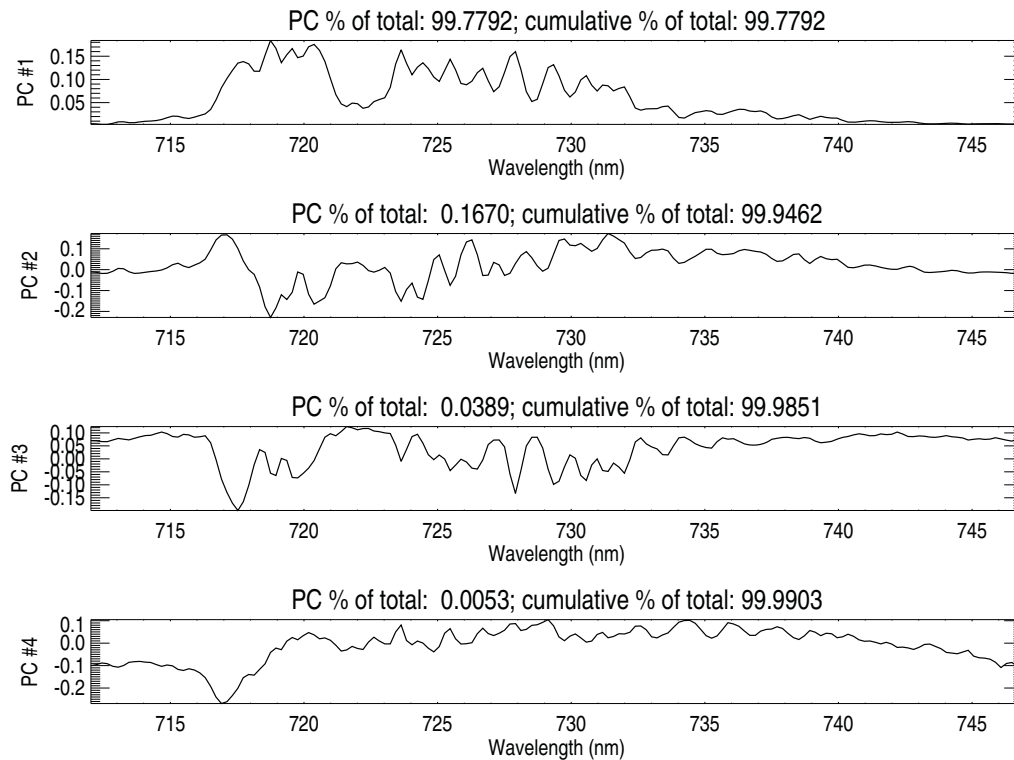


**Fig. 6.** Similar to Fig. 5 but the PCA is conducted using actual GOME-2 data taken over ice- and snow-covered surfaces, the Sahara, and cloudy ocean.

optically thick and absorption is temperature dependent, simulations are needed to evaluate how well our simplified approach will work in this spectral region. Our approach is flexible in that different fitting windows may be utilized. As will be shown below, the O<sub>2</sub> A-band can in fact be completely removed from an extended fitting window without much if any loss of information content.

To the extent that our approach is shown to be successful, there are several advantages. By using PCs, we do not need to estimate parameters affecting O<sub>2</sub> and H<sub>2</sub>O absorption such as surface pressure, temperature and water vapor profiles, and cloud and aerosol parameters that affect nearly all satellite observations. In addition, we eliminate dependence upon a precise specification of the instrument response function. The PCs may also capture instrument artifacts that are otherwise difficult to quantify.

As in DOAS retrievals, we use the logarithm of sun-normalized radiance spectra for the PCA. We first compute PCs with the simulation training data set. For comparison, we also generate PCs using actual GOME-2 satellite radiance data. For the GOME-2 PCA, we use spectra from a single day (1 May 2007) consisting of observations over sea ice, snow/ice-covered land, the Sahara, and cloudy ocean for pixels with  $\theta_0 < 75^\circ$ . For the cloudy ocean data, we compute the reflectance at 670 nm ( $\rho_{670}$ ) and use observations only for  $\rho_{670} > 0.7$ .

For both real and simulated data, we normalize the spectra with respect to a second-order polynomial fit to wavelengths not significantly affected by atmospheric absorption (i.e., 712–713 and 748–757 nm, and wavelengths  $> 775$  nm) before taking the logarithm of the spectra. This normalization produces values representative of the total sun to satellite absorptance. We are able to use a second-order polynomial for this fit of spectra that do not contain complex surface reflectances. However, as noted below, we need to use higher-order polynomials to characterize vegetated surfaces. Alternatively, PCAs may be similarly performed without taking the logarithm of the normalized spectra in order to model transmittance instead of absorptance.

Absorption affecting fluorescence in the far-red emission feature includes that from the O<sub>2</sub> A-band near 760 nm as well as a weaker water vapor band at shorter wavelengths. Figure 4 shows examples of normalized spectra approximating the sun-to-satellite transmittance separately for two wavelength ranges: (1) 712–747 nm, dominated by H<sub>2</sub>O absorption, and (2) 747–783 nm encompassing the O<sub>2</sub> A-band.

Figure 5 shows the leading four PCs for the wavelength range 712–747 nm computed with simulated data for FWHMs of 0.5 nm (similar to GOME-2) and 0.3 nm. The spectral variance in this window is due almost exclusively to water vapor absorption. The variances explained (with respect to the total) as well as the cumulative variances

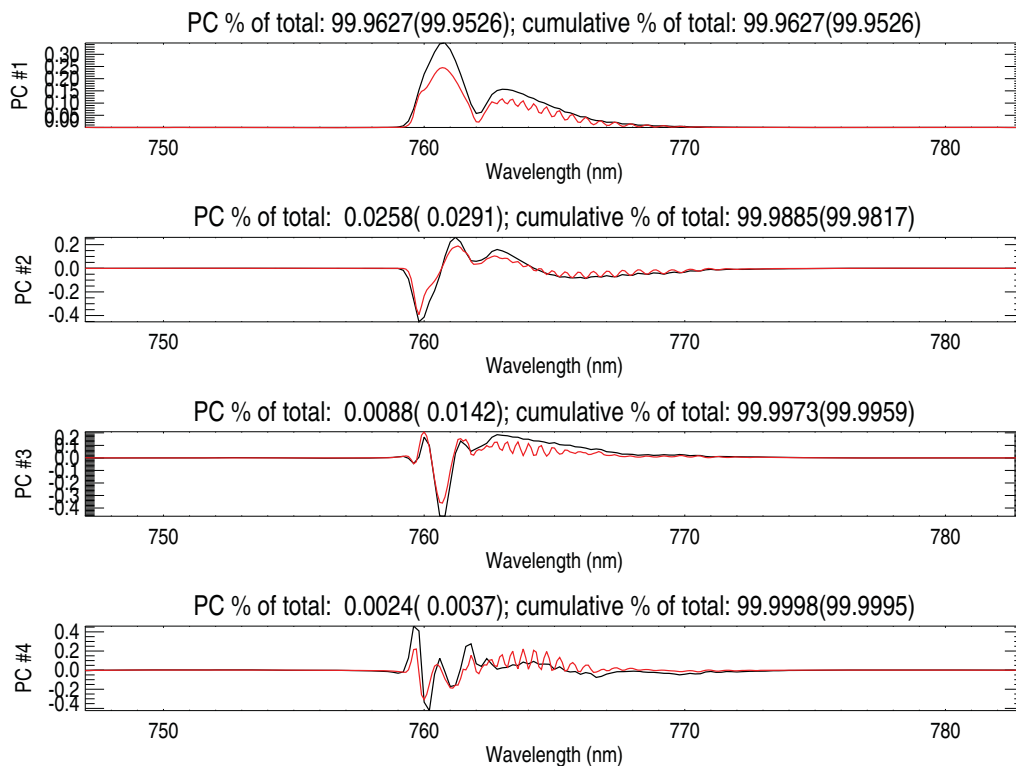


Fig. 7. Similar to Fig. 5 but for the long-wavelength fitting window using simulated data.

explained are indicated. The PCs are similar for the two spectral resolutions with somewhat deeper structures at the higher resolution. The variance explained by the leading PCs is similar for the two spectral resolutions.

Figure 6 similarly shows PCs generated from actual GOME-2 satellite data. PCs and variance explained are similar for the simulated and GOME-2 data. The first PC explains over 99 % of the spectral variance, and 99.99 % of the variance is captured in the first four modes for both the simulated and GOME-2 data. However, PC #4 from GOME-2 appears to correspond to PC #3 from the simulated data, but there is no similar correspondence between PC #3 from GOME-2 and PC #4 from the simulation. The PCs for simulated and real data are expected to be different as PCs from the real data may contain information related to instrumental artifacts and processes not included in the simulated data (e.g., rotational Raman scattering). In addition, the simulated data may not represent all of the conditions or the distribution of conditions that are present in the GOME-2 data, particularly bright scenes that occur over heavily clouded conditions. The training data set, however, does include bright soils and snow.

Figures 7 and 8 similarly show the leading PCs for the spectral window 747–783 nm dominated by strong oxygen A-band absorption near 760 nm. Again, the PCs are similar for simulated and GOME-2 satellite data with over 99.9 % of variance captured by the leading mode, and more than 99.999 % of the variance explained by the first four modes.

PCs #2 and #3 appear to be reversed for the GOME-2 and simulated data.

### 4.3 Solving the nonlinear problem

To solve the nonlinear estimation problem, we use a gradient-expansion algorithm adapted from Marquardt (1963) and Bevington (1969). This algorithm provides a relatively fast convergence, typically 4–6 iterations. We derive and supply to this algorithm the analytic Jacobians or partial derivatives of the observed radiances with respect to the state variables.

Typical Jacobians (i.e., partial derivatives of the reflectances with respect to the coefficients of the PCs, surface reflectance polynomials, and the peak value of the far-red fluorescence feature at 736.8 nm) are shown in Fig. 10 for FWHMs of 0.5 and 0.3 nm. Although the components are not completely orthogonal, our simulation results will show that fluorescence can be successfully disentangled from atmospheric and surface parameters. Subtle differences in the Jacobians enable this differentiation. For example, small Fraunhofer structures can be seen in the fluorescence Jacobian at wavelengths between about 745 and 758 nm that are not seen in the other Jacobians. An instrument with a high enough spectral resolution and SNR should be able to detect these features as will be demonstrated below. Again, deeper spectral structures are seen at the higher spectral resolution.



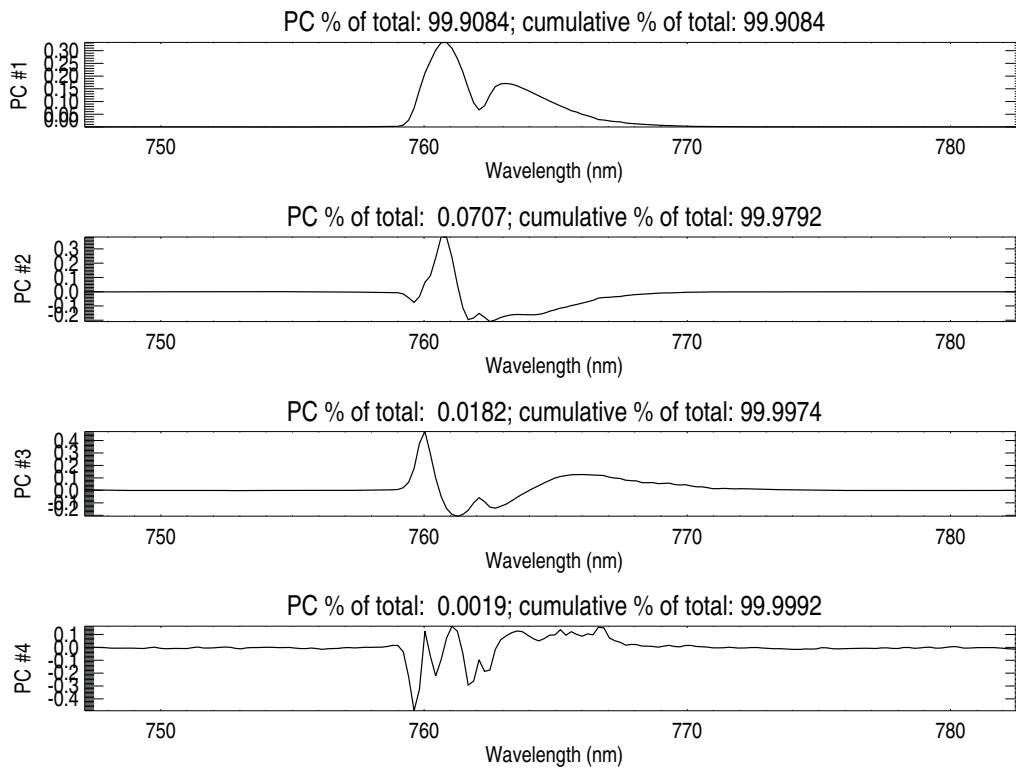


Fig. 8. Similar to Fig. 6 but for the long-wavelength fitting window computed using actual GOME-2 data.

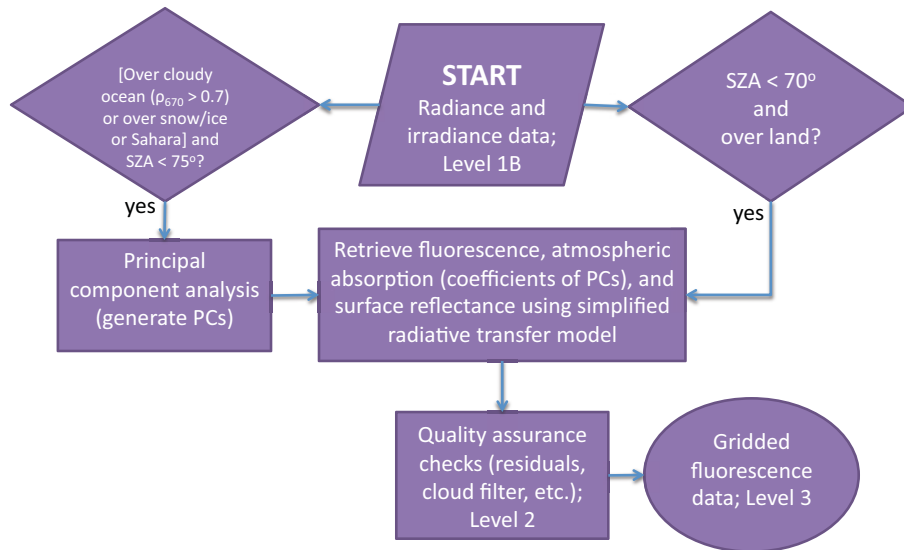
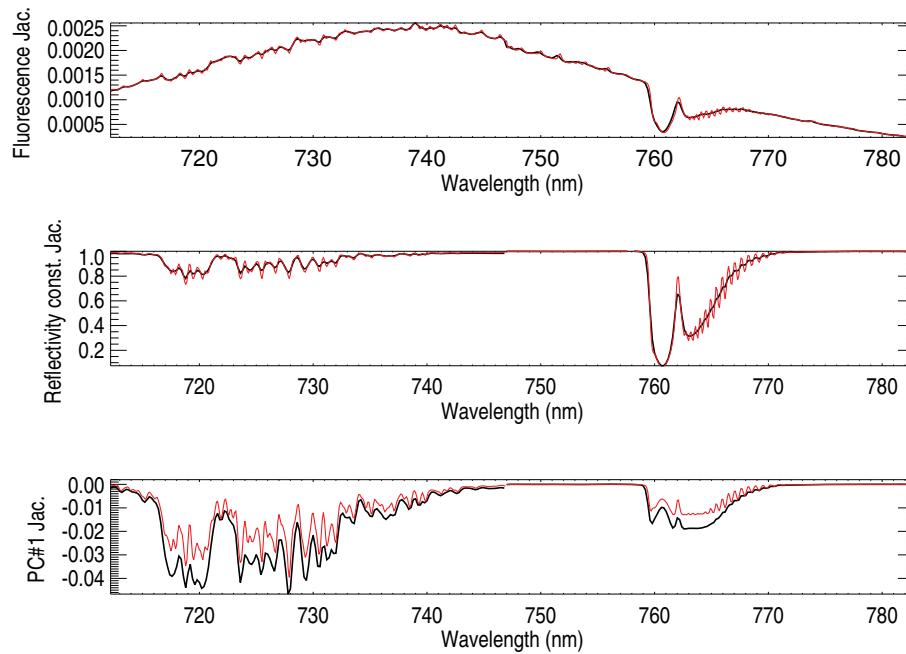


Fig. 9. Flow diagram showing the overall processing scheme for GOME-2 fluorescence retrievals.



**Fig. 10.** Typical Jacobians ( $\partial\rho/\partial x$ ) where  $x$  is the far-red fluorescence peak value (top), the wavelength-independent component of the surface reflectivity (middle), and the coefficient of the first PC (bottom) for FWHM = 0.5 nm (black) and FWHM = 0.3 nm (red). The PC analyses are carried out separately for the wavelength ranges 712–747 nm and 747–783 nm but are shown in a single plot for convenience.

At convergence, the partial derivatives contained in the Jacobian  $\mathbf{K}$  matrix may be used to compute errors from an unconstrained linear error estimation, i.e.,

$$\mathbf{S}_r = (\mathbf{K}^T \mathbf{S}_e^{-1} \mathbf{K})^{-1}, \quad (7)$$

where  $\mathbf{S}_r$  is the retrieval error covariance matrix, and  $\mathbf{S}_e$  is the measurement error covariance. We use this approach to compute fluorescence error standard deviations and correlations and compare these error estimates with those obtained in the full retrieval simulation as will be discussed below. We also use the linear approach to estimate errors from GOME-2 retrievals.

#### 4.4 Processing of GOME-2 data

The overall processing of GOME-2 data follows the flow diagram shown in Fig. 9. One subset of radiance data is used to generate the PCs (chosen such that fluorescence is not present), and a different subset is used for the fluorescence retrievals (data over land). A PCA is conducted daily for each subwindow using the daily measured solar flux. We use data over highly cloudy ocean and snow- and ice-covered surfaces ( $\rho$  at 670 nm > 0.7) and the Sahara for the PCA. The derived PCs are then used for the fluorescence retrieval. Following the retrieval, quality assurance checks are done to remove highly cloudy data and failed retrievals as described in more detail below. Finally, the data are gridded at various temporal resolutions to produce level 3 data sets. More than 5 yr of

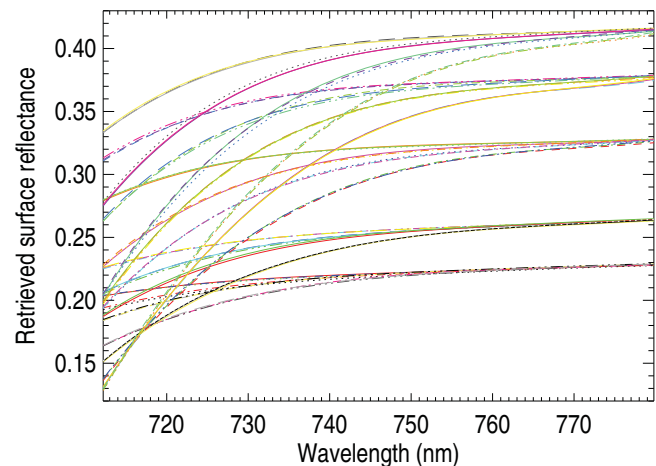


**Fig. 11.** Retrieved spectral surface reflectances for the range of conditions in the simulated data set.

GOME-2 data have been processed, and the level 2 data are available from <http://acdb-ext.gsfc.nasa.gov/People/Joiner/>.

##### 4.4.1 GOME-2 fluorescence retrievals

We use a fitting window from 712 to 783 nm for GOME-2 retrievals with a fourth-order polynomial to model the surface reflectivity and a Gaussian function for the canopy-level far-red fluorescence as described above. We used 25 PCs for each of the two PCA subwindows shown above. No

adjustments are made to the calibrated radiances/irradiance; it should be noted that the MetOp-A GOME-2 is known to have suffered from radiometric degradation over its lifetime.

#### 4.4.2 Cloud filtering and quality control

As in Joiner et al. (2012), we compute the effective cloud fraction  $f_c$  and eliminate data with  $f_c > 0.4$ . To compute  $f_c$ , we use the black-sky 16-day gridded filled-land surface albedo product from Aqua MODIS (MOD43B3) at 656 nm (Lucht et al., 2000). Application of more or less stringent limits on cloud contamination within a moderate range (0–0.5) did not substantially alter the derived spatial and temporal patterns of  $F_s$ , but stricter limits decrease the number of samples included, and therefore reduce coverage and increase noise in the gridded averages.

In the results shown below, we include all data passing gross quality assurance checks on the retrieval convergence and radiance residuals. These checks removed few observations in general. However, the South Atlantic Anomaly (SAA) adds noise to GOME-2 measurements in the vicinity of South America, and most of the data removed by the residual checks were located in this area. The distribution and sampling frequency of the data used to generate the PCs leads to higher retrieval uncertainties than the SAA; the relatively small number of PCs used in the retrieval generally does not capture the highly variable errors found in the region. While many of the affected spectra are screened out by radiance residual checks, the filtering process reduces sampling and may not eliminate all affected spectra. Therefore, GOME-2 errors are generally higher over South America as compared with other areas. We also eliminate all data with  $SZA > 70^\circ$ .

## 5 Sensitivity analysis

In this section, we retrieve fluorescence using the simulated radiances for the 230 400 different conditions contained in the testing data set described in Sect. 3. We conduct retrievals for a number of different scenarios. We then compare the retrieved fluorescence with that of the truth as specified in the testing data set for the entire sample. Table 1 provides statistical results of those comparisons for the scenarios described below.

### 5.1 Sensitivity to number of PCs used

In the first experiment, we simulate data for a fitting window between 747 and 780 nm and for an instrument with  $\text{FWHM} = 0.5$  nm, sampling of 0.2 nm, and  $\text{SNR} = 2000$ . Instrument noise is uncorrelated between channels, and follows a Gaussian distribution. Here, we use a fourth-order polynomial to model the surface reflectivity. Increasing the polynomial order does not significantly improve the results, while use of a second-order polynomial significantly degrades re-

sults. For reference, Fig. 11 displays the range of spectral surface reflectances that are retrieved from the diverse simulated data.

The first four lines of Table 1 show results for retrievals that use 5, 10, 15, and 25 PCs. There are small biases in all cases with biases generally decreasing with increasing numbers of PCs. The improvement in both accuracy and precision is noticeable when increasing from 5 to 10 PCs, and levels out with further increases. There is virtually no change in the results when we increase the number of PCs from 25 to 35 (not shown). We find that a similar number of PCs is needed for the shorter-wavelength subwindow (712–747 nm). For the remainder of this section, all retrievals will use 25 PCs for each of the two subwindows.

We also computed fluorescence errors using the linear estimation method. Here, we assumed random and uncorrelated radiance errors. The radiance errors were also assumed to be independent of wavelength. This is consistent with the errors generated in the simulated data set. We computed errors for the various wavelength ranges, numbers of PCs, and SNRs used above. We find that the computed fluorescence error standard deviations from the linear approach are very close (within  $\sim 4\%$ ) to those obtained in the full retrieval simulation. We find that fluorescence errors can be moderately correlated with errors in the constant reflectivity term and some of the leading PCs.

### 5.2 Sensitivity to signal-to-noise ratio

For comparison, Table 1 shows results of fluorescence retrievals using simulated observations as above with  $\text{SNR} = 1000$ . Results may be compared with the 25 PC case (line 4) described in Sect. 5.1 for an instrument with  $\text{SNR} = 2000$ . Standard deviations and root-mean-squared (RMS) errors for  $\text{SNR} = 1000$  are slightly less than twice those at  $\text{SNR} = 2000$ . This is consistent with the expected behavior of a retrieval based solely on solar Fraunhofer line structure, where errors are inversely proportional to SNR with all other parameters held constant (Joiner et al., 2012).

### 5.3 Sensitivity to the fitting window

In the experiments shown in lines 6–10 of Table 1, we use different fitting windows for an instrument with  $\text{SNR} = 2000$  and  $\text{FWHM} = 0.5$  nm. Fluorescence errors are approximately a factor of 2 smaller with the 712–747 nm fitting window as compared with the 747–780 nm shown above. This demonstrates that fluorescence retrievals can be obtained with good precision without using the filling-in signal from the O<sub>2</sub> A-band. The 712–747 nm window spans the peak far-red fluorescence, and also contains H<sub>2</sub>O absorption. A reduced fitting window of 723–747 nm produces slightly degraded results as compared with the 712–747 nm window. Both of these shorter-wavelength windows show decreased bias as compared with the 747–780 nm window that includes the O<sub>2</sub>

**Table 1.** Statistical comparison of retrieved versus true values of  $F_s$  obtained with the simulated testing data set for different experiments (Exp); all fluorescence radiance units (indicated by \*) are  $\text{mW m}^{-2} \text{nm}^{-1} \text{sr}^{-1}$ . Retrievals are performed for an instrument with a given full-width-at-half-maximum (FWHM) line shape function, signal-to-noise ratio (SNR), number of principal components (#PCs), and fitting window from starting wavelength  $\lambda_1$  to ending wavelength  $\lambda_2$ . Statistics given are the root-mean-squared difference (RMS diff.), correlation coefficient ( $r$ ), mean difference (bias) of retrieved minus truth, standard deviation ( $\sigma$ ), and slope (A) and intercept (B) of a linear fit (retrieved fluorescence =  $A + B \cdot \text{truth}$ ) (last two columns).

Exp	FWHM (nm)	SNR	#PCs	$\lambda_1$ (nm)	$\lambda_2$ (nm)	RMS diff. *	$r$	bias *	$\sigma$ *	slope	intercept *
1	0.5	2000	5	747	780	0.88	0.67	-0.68	0.57	0.43	-0.03
2	0.5	2000	10	747	780	0.58	0.82	-0.37	0.45	0.58	0.11
3	0.5	2000	15	747	780	0.50	0.87	-0.32	0.38	0.72	-0.01
4	0.5	2000	25	747	780	0.43	0.87	-0.22	0.38	0.80	0.01
5	0.5	1000	25	747	780	0.70	0.69	-0.22	0.67	0.80	0.01
6	0.5	2000	25	712	747	0.33	0.97	-0.07	0.32	1.00	0.07
7	0.5	2000	25	723	747	0.37	0.97	-0.01	0.37	0.94	0.13
8	0.5	2000	25	755	775	0.56	0.76	-0.30	0.47	0.71	0.01
9	0.5	2000	25	759	768	1.19	0.43	-0.46	1.10	0.70	-0.13
10	0.5	2000	25	747	758	1.48	0.58	-0.03	1.48	0.98	0.01
11	0.3	2000	25	747	780	0.49	0.85	-0.29	0.40	0.80	-0.06
12	0.3	2000	25	712	747	0.22	0.99	-0.11	0.19	0.94	0.02

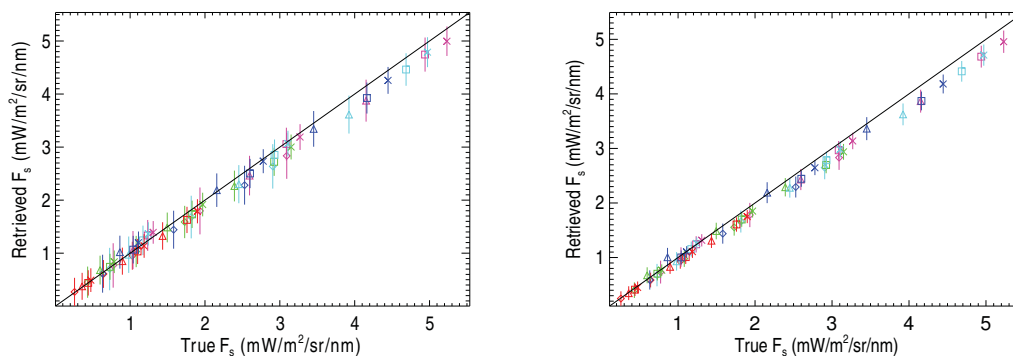


**Fig. 12.** Fluorescence retrievals from simulated data (y axis) using wavelengths between 712 and 747 nm for instruments with FWHM = 0.5 nm (left) and FWHM = 0.3 nm (right), both with a signal-to-noise ratio of 2000. Fluorescence is averaged over the wavelengths used in the retrieval and compared with the “truth” (x axis) averaged in the same way. Standard deviations are shown with vertical bars. Different symbols are shown for the various values of chlorophyll content, and different colors are for the different values of leaf area index.

A-band. Our results are consistent with those of Guanter et al. (2013), who similarly showed that fitting windows in this spectral region, without the benefit of the O<sub>2</sub> A-band, can be used to retrieve fluorescence with higher-spectral-resolution ground-based instruments.

Table 1 also examines results for fitting windows more confined to the O<sub>2</sub> A-band. As may be expected, retrievals are degraded for a smaller fitting window of 755–775 nm as compared with the 747–780 nm window used above. Results are also shown with a smaller fitting window of 759–768 nm. This window consists primarily of the O<sub>2</sub> A-band with embedded Fraunhofer structure. Note that the strongest solar Fraunhofer feature within the range 712–783 nm occurs inside the O<sub>2</sub> A-band region near 766 nm. Results are significantly degraded with this limited fitting window. Franken-

berg et al. (2011a) noted the difficulties associated with disentangling fluorescence spectral information from that of aerosols, clouds, surface pressure, etc., using only wavelengths within O<sub>2</sub> A-band spectral region. Although there is a significant correlation between fluorescence and these other parameters, there is nevertheless a limited ability to retrieve information about fluorescence within this absorption band. However, biases increase as the fitting window is more confined to the O<sub>2</sub> A-band spectral region. Precision is significantly degraded with a limited fitting window of 747–758 nm containing only weak solar Fraunhofer line structures, while the accuracy for this fitting window is good.

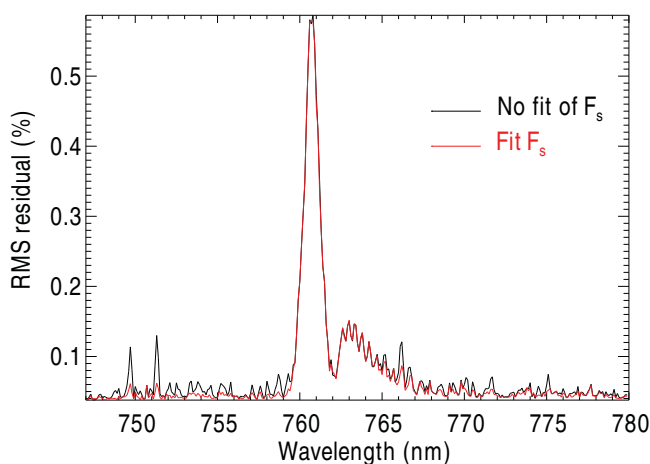


**Fig. 13.** RMS of simulated radiance residuals (in percent of radiance) from the testing data set with FWHM = 0.3 nm and SNR = 2000 when fluorescence radiance ( $F_s$ ) is fitted/retrieved and when it is not fitted/retrieved.

#### 5.4 Sensitivity to spectral resolution

In order to show the sensitivity of the results to spectral resolution, we performed a similar set of experiments at a higher spectral resolution (FWHM = 0.3 nm, sampling of 0.1 nm) as compared with that used in the above subsections. Lines 12 and 13 of Table 1 show retrieval statistics for the higher-spectral-resolution instrument with SNR of 2000 for fitting windows of 747–780 nm and 712–747 nm, respectively. The precision is significantly improved as compared with FWHM = 0.5 nm retrievals. This improvement results from (1) more spectral samples within the fitting window and (2) a larger filling-in fluorescence signal in the cores of the deeper Fraunhofer lines that are better resolved at the higher spectral resolution as shown in Fig. 10. Further improvements can be made by making measurements with higher spectral resolution and/or increased sampling. We also varied the fitting window as in Sect. 5.3 for FWHM = 0.3 nm, and reached the same conclusions as with FWHM = 0.5 nm.

As described above, there are 60 distinct values of fluorescence (averaged between 740 and 780 nm) ranging from near zero to near  $4 \text{ mW m}^{-2} \text{ nm}^{-1} \text{ sr}^{-1}$ . For each value, the observing conditions vary (e.g., different SZAs, VZAs, surface pressures, temperature profiles, and aerosol parameters). Figure 12 shows retrieval results using the 712–747 nm fitting window for the FWHM = 0.3 and 0.5 nm simulated data with SNR = 2000. This figure shows that biases are more prevalent for higher levels of fluorescence.

#### 5.5 Radiance residuals from simulated data

Figure 13 shows RMS of the radiance residuals (observed minus calculated radiance) for two cases with FWHM = 0.3 nm, SNR = 2000, and a fitting window of 747–

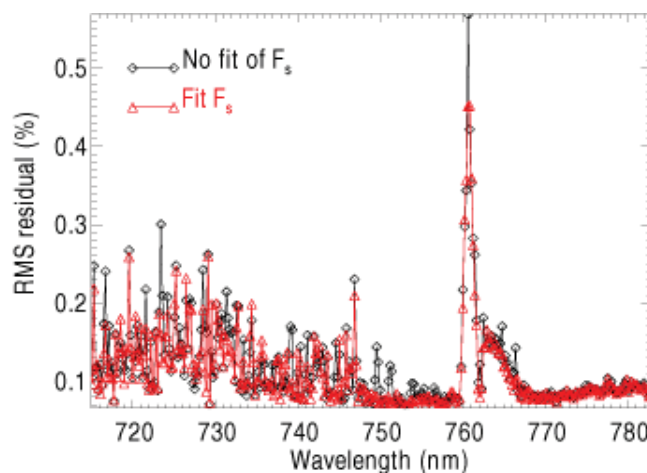


**Fig. 14.** RMS of GOME-2 radiance residuals obtained with and without fitting  $F_s$  (in percent of the observed radiance) for a single day for moderately to highly vegetated pixels.

780 nm: (1) fluorescence is not retrieved, and (2) fluorescence is retrieved. The RMS of the residual is computed at each wavelength averaged over all conditions in the simulation testing data and shown as a percentage of observed radiance. As expected, reductions in the residuals are achieved when fluorescence is retrieved, particularly in the vicinity of deep solar Fraunhofer lines (e.g., near 749, 751, and 766 nm). These improvements occur throughout the full spectral range.

We conducted an additional experiment in which we use a flat solar spectrum in place of the simulated solar spectrum with the fitting range 747–780 nm that includes the O<sub>2</sub> A-band. We obtained poor results with our retrieval approach when using the flat solar spectrum (essentially no information about  $F_s$  is retrieved). This is another indicator that our method relies primarily on the filling-in of solar Fraunhofer lines to retrieve  $F_s$ .

Note that relatively larger residuals (larger than instrument noise but well below 1 %) are produced at the very low radiance levels found within the deep O<sub>2</sub> A-band. This result is seen in both the simulated data as well as real GOME-2 data as will be shown below. These residuals could be the result of nonlinear behavior of the O<sub>2</sub> A-band that the PCA method is not able to capture.

#### 5.6 Discussion of simulation results

As noted above, our retrieval approach relies on several simplifying assumptions. For example, we assume that atmospheric scattering is negligible, that the radiative transfer assumptions are only valid for monochromatic light, and that the spectral structures of  $F_s$  and  $\rho_s$  could be modeled with a few parameters. The simulated data contain none of these assumptions; the radiances are generated monochromatically with scattering before they are convolved with the instrument

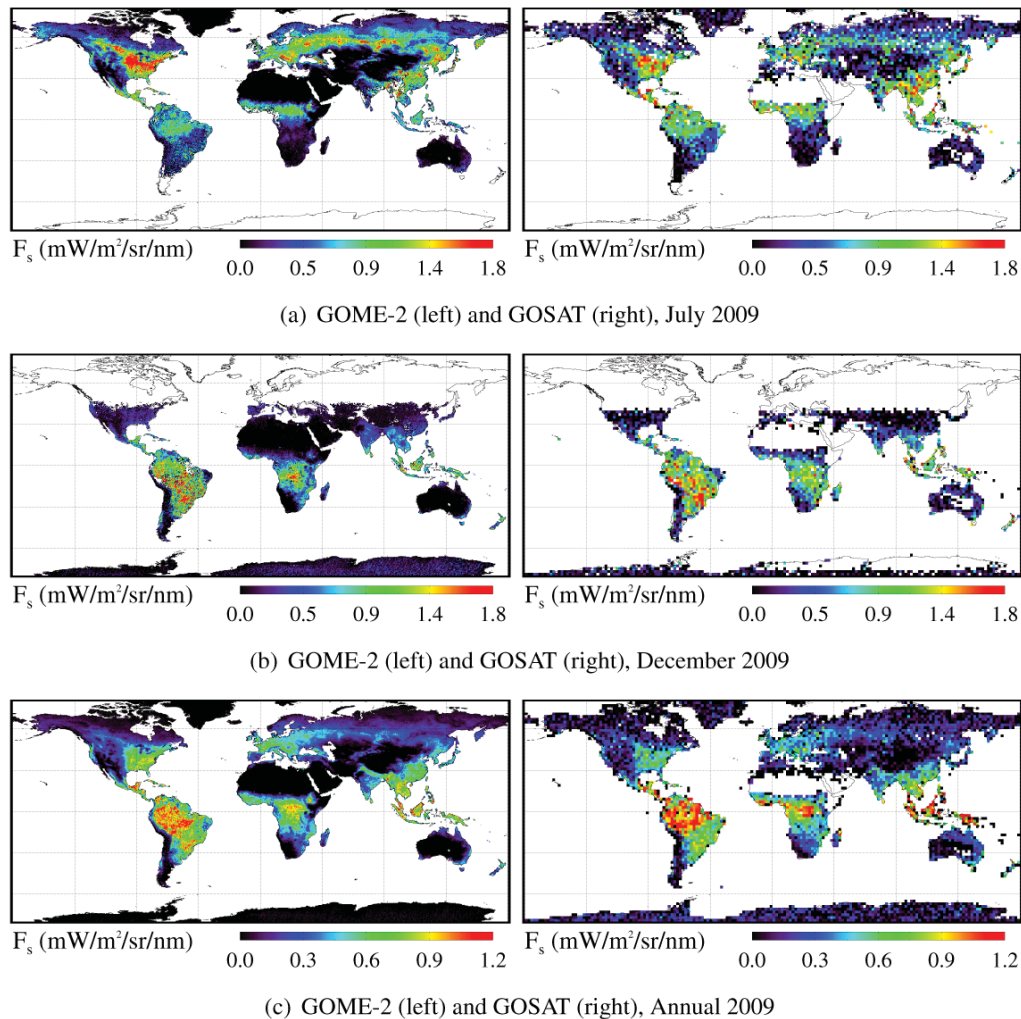


**Fig. 15.** Global composites of  $F_s$  from GOME-2 (left) and GOSAT-FTS (right) retrievals for July (top), December (middle) and the annual (bottom) average in 2009 (June 2009 through May 2010 for GOSAT). GOME-2 are binned in  $0.5^\circ$  cell boxes; GOSAT retrievals binned in  $2^\circ$  cell boxes. Both retrievals refer to wavelengths near 757 nm.

response function, and the spectral dependences of  $F_s$  and  $\rho_s$  are based on model and spectral libraries. Therefore, our simulation results should accurately reflect errors produced by these assumptions. As can be seen, the biases and errors produced by these simplifications are relatively small. We did not simulate RRS in the simulation. Our assumption in processing GOME-2 data is that the PCA will be able to disentangle the spectral effects of RRS from those of  $F_s$ . This will be discussed further below.

## 6 Results from GOME-2 data

### 6.1 Radiance residuals from GOME-2

Figure 14 shows the spectral RMS of the radiance residuals, obtained with and without fitting  $F_s$ , over the GOME-2 fitting window for a single day. Residuals are averaged

for each wavelength over all observations with  $\text{SZA} < 70^\circ$  and  $\text{NDVI} > 0.3$  (i.e., moderately to highly vegetated pixels) that passed quality-control and cloud-filtering checks. Reductions in the residuals can be seen throughout the spectral range with a similar spectral structure as shown in Fig. 13 for the simulated data (i.e., reductions at the deep solar Fraunhofer lines). Some reduction is also seen at the deepest part of the O<sub>2</sub> A-band near 760 nm. In the portions of the fitting window that are relatively free of atmospheric absorption, the residuals are consistent with a GOME-2 SNR of 1000 or greater. Residuals have similar magnitudes to those shown in Fig. 13 for simulated data with  $\text{SNR} = 2000$ . Residuals are somewhat higher in regions where atmospheric absorption is present such as in the water vapor absorption band shortward of about 747 nm.

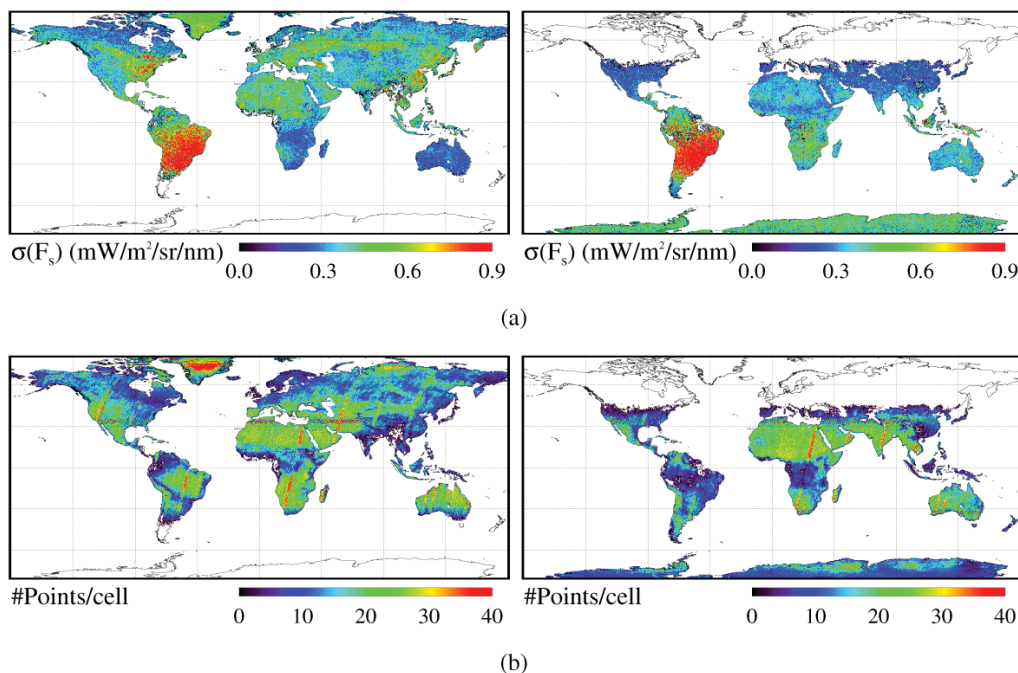


**Fig. 16.** Global maps of GOME-2  $F_s$  retrieval statistical parameters in a  $0.5^\circ$  grid cell for July (left column) and December (right column) 2009. Each column shows the standard deviation (top) and the number of points per grid cell (bottom).

## 6.2 Comparison of GOME-2 and GOSAT fluorescence

Global composites of  $F_s$  derived from GOME-2 for July, December and the annual average in 2009 are displayed in Fig. 15. Here, we converted the retrieved peak values of fluorescence at 736.8 nm to values that would have been observed at the GOSAT wavelengths (near 759 nm). We multiplied the 736.8 nm fluorescence by a factor of 0.59. This factor is consistent with the spectral shape of the fluorescence emission assumed in the retrievals. It is also consistent with the fluorescence emissions used in the simulated testing data set (see Fig. 3). For comparison, maps of  $F_s$  at 757 nm from GOSAT-FTS retrievals are also shown for the same time periods (the annual average is from June 2009 through May 2010 for GOSAT). The GOSAT-FTS retrievals were performed and processed with the algorithm described in Guanter et al. (2012). Quality-filtered GOME-2 retrievals have been averaged in  $0.5^\circ$  latitude-longitude grid boxes, whereas a  $2^\circ$  grid is used for the GOSAT retrievals that have a much more sparse spatial sampling than GOME-2. The filtering uses data only for  $\text{SZA} < 70^\circ$ , where RRS effects should be small. We see no obvious biases resulting from RRS for these conditions.

A very good agreement of the  $F_s$  spatial patterns is observed between the two data sets, although improvements in spatial resolution and precision are obvious in the GOME-2 maps. High  $F_s$  values are observed over densely vegetated areas. Globally, the highest  $F_s$  signal is found in July in the eastern United States. High  $F_s$  values are also observed

in some parts of South America and Africa in December. In some of these regions, GOME-2 values are higher than GOSAT. This may be the result of differences in absolute calibration of the instruments or small biases in the GOME-2 algorithm. The higher GOME-2 values are inconsistent with the differences due to time of day and cloud contamination as discussed in more detail below.

$F_s$  values near zero are detected in July over Greenland (zero to slightly negative), in December over Antarctica (zero to slightly positive), and during the entire year over the Sahara and most of Australia. These spatial patterns compare well with those observed in the  $F_s$  maps derived from GOSAT-FTS for the same time periods. The slight biases (both positive and negative) in these areas are likely not related to random instrumental noise as this would be removed in a long-term average. There are several potential sources of these small biases, including simplifying assumptions in the forward model, small correlations between the fluorescence spectral signal and that of reflectivity and/or some of the PCs, lack of representativeness of the PCs used in the retrieval, and systematic instrumental artifacts.

Concerning the annual averages of  $F_s$  retrievals, the main difference between the two data sets is in the tropical rainforest, especially in Africa and Indonesia. GOME-2  $F_s$  is, in relative terms, lower than that of GOSAT over those areas. This may be due to a larger impact of cloud contamination in coarser GOME-2 footprint data ( $40 \text{ km} \times 80 \text{ km}$  for GOME-2 as compared with an around  $10 \text{ km}$  diameter for GOSAT). The smaller footprint of GOSAT may also allow for higher

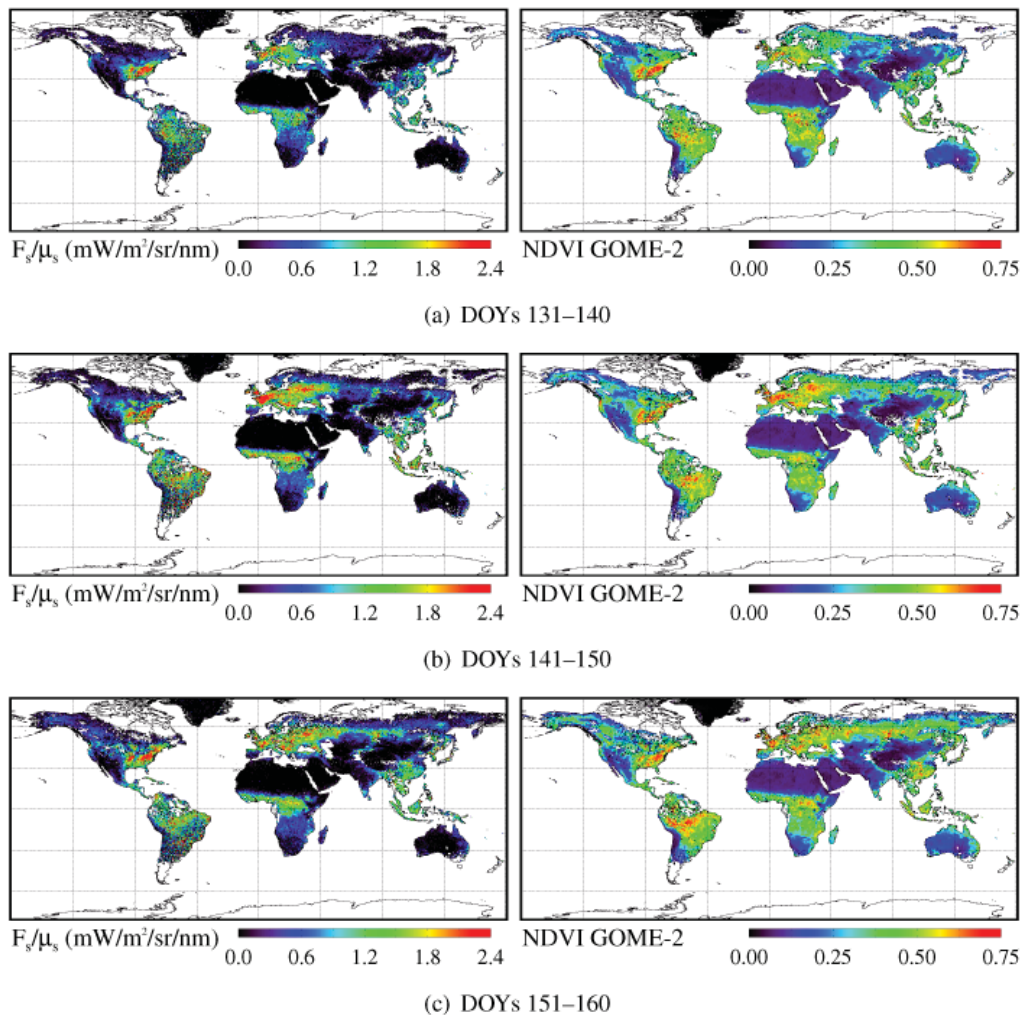


**Fig. 17.** Ten-day composites of  $F_s$  and NDVI derived from GOME-2 data in  $0.5 \times 0.5^\circ$  grid cells between day of year (DOY) 131 and 160 of 2009. Fluorescence is normalized by the cosine of the sun zenith angle ( $\mu_s$ ) in order to minimize the temporal and latitudinal dependence of fluorescence on incoming at-surface photosynthetically active radiation.

peak values of  $F_s$  signals to be obtained in areas of very dense productive vegetation. At the same time, the low sampling of GOSAT may not allow for adequate representation of grid-box averages.

The different solar illumination angles encountered by the two instruments may also contribute to relative differences between high and low latitudes. The overpass time of the satellites ( $\sim 09:30$  LT for MetOp-A,  $\sim 13:00$  LT for GOSAT) results in GOME-2 measurements that have systematically higher solar zenith angles (SZAs) as compared with GOSAT. In general, the illumination angle affects the fluorescence signal at the top of canopy through (1) the intensity of the sunlight incident at the canopy; (2) the amount of illuminated leaves that is related to the ratio of diffuse-to-direct irradiance; and (3) the physiological relationship between photosynthesis, fluorescence, and heat dissipation.

The overall excellent spatial agreement between GOME-2 and GOSAT can be considered as a rough first validation of our GOME-2  $F_s$  retrievals given the fact that the GOME-2 retrieval approach is much more complicated and prone to systematic errors as compared with that of GOSAT. While the GOME-2/GOSAT comparison may be considered as a consistency check and the simulation experiments provide evidence that the retrieval approach is valid, there are shortcomings to these types of evaluations. Firstly, the GOSAT retrievals themselves have only been evaluated using indirect strategies such as plausibility checks and simulation experiments. Secondly, the simulation studies, while quite detailed, generally do not contain all the complexities found in real satellite data (e.g., instrumental artifacts and RRS). A more direct validation using ground- and aircraft-based data remains challenging owing to the large pixel sizes of the current satellite instruments. Approaches need to be developed



and tested to scale up measurements made at small scales (ground-, aircraft-, and small-footprint satellite data) to the larger GOME-2 pixels.

### 6.3 Estimated errors, variability, and numbers of GOME-2 retrievals

The standard deviation of the July and December  $F_s$  retrievals in Fig. 16a indicates the variability of the  $F_s$  values observed in each  $0.5^\circ \times 0.5^\circ$  gridbox. Sources of this variability are instrumental noise, natural variability in vegetation activity within the month, residual cloud effects, variability owing to different illumination and viewing geometries, and the different footprints from various MetOp-A orbits. We have observed systematic variability with respect to view zenith angle for a given area over the course of a month as has been reported previously for GOSAT and SCIAMACHY data (Guanter et al., 2012; Joiner et al., 2012). The analysis of the effects of the illumination and viewing geometries on the  $F_s$  signal will be explored in future works.

It can be seen that the highest variability in the retrievals is found over a large area in South America, and that this does not depend on the season. Instrument performance in this region is substantially degraded by the SAA. Even though this effect does not appear to have a large impact on the monthly average in Fig. 15a and b, the data over this area must be handled carefully. Concerning the rest of the globe, the standard deviation patterns compare well with the expected at-sensor radiance patterns (e.g., higher standard deviations over bright snow-covered areas and deserts) that can be explained by the higher contribution of photon noise triggered by higher at-sensor radiance levels.

We estimated errors based on the linear approach described above assuming random and uncorrelated radiance errors with a signal-to-noise ratio of 1000 consistent with the radiance residual analysis. We obtained fluorescence standard deviation values similar to the variability shown in Fig. 16 (estimated standard deviations of  $\sim 0.4$ – $1 \text{ mW m}^{-2} \text{ nm}^{-1} \text{ sr}^{-1}$  in moderately to heavily vegetated areas). However, the linear error estimates were higher than the variability shown over surfaces with high reflectivity including Greenland and the Sahara region. Estimated errors in these areas can exceed  $1.5 \text{ mW m}^{-2} \text{ nm}^{-1} \text{ sr}^{-1}$ . This may indicate that the SNR of GOME-2 is higher for these bright scenes as compared with other areas. Error estimates were lower than the variability shown in the region of the SAA, because the increased noise in this area was not accounted for in the linear estimation.

Figure 16b shows the number of  $F_s$  retrievals fulfilling the quality criteria per gridbox. Note that the red orbital stripes are not artifacts but are due to narrow swath data that are obtained approximately once per month. Typically, 10–25 retrievals are available for each grid box within a month. Those numbers are smaller over highly cloudy tropical rainforest regions, especially during the wet season in Decem-

ber, and at high latitudes. Therefore, fluorescence standard errors for the monthly mean gridded data are reduced by factors between approximately 3 and 5 as compared with the estimated single observation error. Estimated fluorescence errors for monthly mean gridded data are in the range  $0.1$ – $0.4 \text{ mW m}^{-2} \text{ nm}^{-1} \text{ sr}^{-1}$ .

### 6.4 Temporal variations in GOME-2 fluorescence and NDVI

The high revisit time of GOME-2 allows for excellent temporal sampling in the derived vegetation products. This is illustrated in Fig. 17. The figure shows 10-day composites of  $F_s$  and NDVI derived from GOME-2 data between day of year (DOY) 131 (11 May) and 160 (10 June) of 2009. Here, fluorescence values are normalized by the cosine of the solar zenith angle in order to minimize the latitudinal and temporal variations in fluorescence owing to the incoming PAR. A lower signal-to-noise ratio is observed for these 10-day composites as compared with the monthly averages in Fig. 15, especially in the area of the South American region affected by the SAA. Spatial gaps in the data are due to persistent cloud contamination, as MetOp provides near-daily global coverage.

We use a standard definition to compute NDVI from GOME-2, i.e.,

$$\text{NDVI} = \frac{\rho_{\text{NIR}} - \rho_{\text{RED}}}{\rho_{\text{NIR}} + \rho_{\text{RED}}}, \quad (8)$$

where the  $\rho_{\text{NIR}}$  and  $\rho_{\text{RED}}$  are computed using single wavelength observations closest to 780 and 670 nm, respectively. Note that the values of  $\rho_{\text{NIR}}$  and  $\rho_{\text{RED}}$  have not been corrected for atmospheric scattering, surface BRDF effects, or fluorescence, and are affected by cloud contamination within the GOME-2 footprint. Despite the simplicity of the GOME-2 NDVI calculation, spatial patterns are similar to those of the MODIS NDVI product (not shown). The GOME-2 NDVI sampling is identical to that of the GOME-2 fluorescence.

Phenological changes in the Northern Hemisphere are clearly visible from one 10-day period to another in Fig. 17. A strong increase in  $F_s$  is observed in Europe from DOYs 131–140 to DOYs 141–150. This rapid change in green biomass is also detectable in the NDVI, although with a smaller intensity. This high temporal sampling of  $F_s$  trends cannot be achieved with GOSAT data owing to the significantly lower number of observations and the sparse spatial sampling. Improved temporal sampling should be achievable by processing data from both GOME-2 instruments for the periods of dual measurements.

## 7 Conclusions

We have developed a new approach to retrieve far-red fluorescence from moderate-spectral-resolution satellite instruments. The method utilizes fluorescence filling-in of the O<sub>2</sub>

A and water vapor bands as well as the surrounding weak solar Fraunhofer lines; it relies upon the separation of spectral signatures produced by upwelling chlorophyll fluorescence and atmospheric absorption as well as surface, cloud, and aerosol backscattering of solar radiation. We use principal components, derived from data free of fluorescence, to estimate the spectral structure of atmospheric absorption. This information is incorporated into a simplified radiative transfer model that accounts for atmospheric absorption of fluorescence emissions. Through detailed simulations, we show that high-quality fluorescence retrievals can be obtained using instrumentation with high SNR and moderate spectral resolution similar to GOME-2. Retrieval errors depend upon the instrument SNR, spectral resolution, and specification of the spectral fitting window.

We then applied our new approach to satellite moderate-spectral-resolution measurements from GOME-2. The GOME-2 retrievals compare well with those from GOSAT that are processed with a less complex algorithm, providing further confidence in our approach and implementation with real data. Fluorescence errors for monthly mean gridded data are estimated to be  $\sim 0.1\text{--}0.4 \text{ mW m}^{-2} \text{ nm}^{-1} \text{ sr}^{-1}$ . Owing to the excellent spatial sampling and high signal-to-noise ratio of the GOME-2 measurements, we are able to map far-red terrestrial fluorescence at higher spatio-temporal resolutions than previously published GOSAT and SCIAMACHY data. This mapping shows clearly for the first time a northward shift in PAR-normalized fluorescence within the single month of May as the sun shifts northward during the boreal spring.

Several satellite instruments with NIR spectral coverage and various spectral and spatial resolutions have flown, are currently flying, or are planned for launch in the next few years. The approach outlined here can potentially be applied to these instruments. SCIAMACHY provides observations in the same spectral region. While the native SCIAMACHY footprint ( $30 \text{ km} \times 60 \text{ km}$ ) is slightly smaller than that of GOME-2 ( $40 \text{ km} \times 80 \text{ km}$ ), the spatial sampling of SCIAMACHY is not as good as GOME-2, in part due to alternating between limb and nadir measurements. In addition, SCIAMACHY observations in the near-infrared at some wavelengths were spatially coadded and are not provided at full spatial resolution in the level 1b data set. The original GOME instrument, launched in 1995 on the European Space Agency's European Remote Sensing satellite 2 (ERS-2), can also be used for fluorescence measurements, but with a larger pixel size ( $40 \text{ km} \times 320 \text{ km}$ ) in its nominal operating mode. SCIAMACHY and GOME have the unique ability to extend the record of fluorescence measurements back to 1995. In addition to GOME-2 and SCIAMACHY, the approach may also be applied to the GOSAT interferometer, the Orbiting Carbon Observatory-2 (OCO-2) (Crisp et al., 2004), planned for launch in 2014, and the Tropospheric Monitoring Instrument (TROPOMI) (Veefkind et al., 2012) to be launched in 2015. The Fluorescence Explorer (FLEX)

(Rascher, 2007; European Space Agency, 2008), an ESA Explorer 8 mission, selected for Phase A/B1 in early 2011, plans to utilize the O<sub>2</sub> A- and B-bands for chlorophyll fluorescence retrievals (Guanter et al., 2010) and other bio-spectral information across the visible through NIR spectral range. FLEX would provide measurements at a higher spatial resolution than current satellite sensors that were not designed for fluorescence measurements.

*Acknowledgements.* Funding for this work was provided by the NASA Carbon Cycle Science program (NNH10DA001N) managed by Diane E. Wickland and Richard Eckman and by the Emmy Noether Programme (GlobFluo project) of the German Research Foundation. The authors are indebted to Phil Durbin and his team for assistance with the satellite data sets, particularly the GOME-2 data. We gratefully acknowledge the European Meteorological Satellite (EUMetSat) program, the GOSAT project, and the MODIS data processing team for making available the GOME-2, GOSAT, and MODIS data, respectively, used here. We also thank William Cook, Yen-Ben Cheng, Qingyuan Zhang, Jianping Mao, Rose Munro, Rüdiger Lang, Petya Campbell, Lawrence Corp, Wouter Verhoef, and Arlindo da Silva for helpful discussions, and Piet Stammes and an anonymous reviewer for comments that helped to improve the manuscript. This work was enabled by collaborations forged at the fluorescence workshop held at the California Institute of Technology Keck Institute for Space Studies, funded by the W. M. Keck Foundation. We gratefully acknowledge the organizers of this workshop including Joseph Berry, Paul Wennberg, and Michele Judd.

Edited by: P. Stammes

## References

- Amoros-Lopez, J., Gomez-Chova, L., Vila-Frances, J., Alonso, L., Calpe, J., Moreno, J., and del Valle-Tascon, S.: Evaluation of remote sensing of vegetation fluorescence by the analysis of diurnal cycles, *Int. J. Remote Sens.*, 29, 5423–5436, 2008.
- Bevington, P. R.: Data reduction and error analysis for the physical sciences, McGraw Hill, 1969.
- Callies, C., Corpaccioli, E., Eisinger, M., Hahne, A., and Lefebvre, A.: GOME-2 – MetOp's Second-Generation Sensor for Operational Ozone Monitoring, available at: <http://esamultimedia.esa.int/docs/metop/GOME-2-102.pdf> (last access: 13 April 2013), *ESA Bull.-Eur. Space*, 103, 28–36, 2000.
- Campbell, P. K. E., Middleton, E. M., Corp, L. A., and Kim, M. S.: Contribution of chlorophyll fluorescence to the apparent vegetation reflectance, *Sci. Total Environ.*, 404, 433–439, 2008.
- Chance, K. and Kurucz, R. L.: An improved high-resolution solar reference spectrum for Earth's atmosphere measurements in the ultraviolet, visible, and near infrared, *J. Quant. Spectrosc. Ra.*, 111, 1289–1295, 2010.
- Corp, L. A., McMurtrey, J. E., Middleton, E. M., Mulchi, C. L., Chappelle, E. W., and Daughtry, C. S. T.: Fluorescence sensing systems: in vivo detection of biophysical variations in field corn due to nitrogen supply, *Remote Sens. Environ.*, 86, 470–479, 2003.

- Corp, L. A., Middleton, E. M., McMurtrey, J. E., Campbell, P. K. E., and Butcher, L. M.: Fluorescence sensing techniques for vegetation assessment, *Appl. Optics*, 45, 1023–1033, 2006.
- Crisp, D., Atlas, R. M., Breon, F.-M., Brown, L. R., Burrows, J. P., Ciais, P., Connor, B. J., Doney, S. C., Fung, I. Y., Jacob, D. J., Miller, C. E., O'Brien, D., Pawson, S., Rander-son, J. T., Rayner, P., Salawitch, R. J., Sander, S. P., Sen, B., Stephens, G. L., Tans, P. P., Toon, G. C., Wennberg, P. O., Wofsy, S. C., Yung, Y. L., Kuang, Z., Chudasama, B., Sprague, G., Weiss, B., Pollock, R., Kenyon, D., and Schroll, S.: The Orbiting Carbon Observatory (OCO) mission, *Adv. Space Res.*, 34, 700–709, 2004.
- Damm, A., Elbers, J., Erler, A., Gioli, B., Hamdi, K., Hutjes, R. W. A., Kosvancova, M., Meroni, M., Miglietta, F., Mersch, A., Moreno, J., Schickling, A., Sonnenschein, R., Udelhoven, T., Van Der Linden, S., Hostert, P., and Rascher, U.: Remote sensing of sun-induced fluorescence to improve modeling of diurnal courses of gross primary production (GPP), *Global Change Biol.*, 16, 171–186, 2010.
- Daumard, F., Champagne, S., Fournier, A., Goulas, Y., Ounis, A., Hanocq, J.-F., and Moya, I.: A field platform for continuous measurement of canopy fluorescence, *IEEE T. Geosci. Remote.*, 48, 3358–3368, 2010.
- European Space Agency: ESA SP-1313/4 Candidate Earth Explorer Core Missions – Reports for Assessment: FLEX – FLuorescence EXplorer, published by ESA Communication Production Office, Noordwijk, the Netherlands, available at: [http://esamultimedia.esa.int/docs/SP1313-4\\_FLEX.pdf](http://esamultimedia.esa.int/docs/SP1313-4_FLEX.pdf) (last access: 13 April 2013), 2008.
- Fell, F. and Fischer, J.: Numerical simulation of the light field in the atmosphere–ocean system using the matrix–operator method, *J. Quant. Spectrosc. Ra.*, 69, 351–388, 2001.
- Flexas, J., Escalona, J. M., Evain, S., Gulías, J., Moya, I., Osmond, C. B., and Medrano, H.: Steady-state chlorophyll fluorescence (Fs) measurements as a tool to follow variations of net CO<sub>2</sub> assimilation and stomatal conductance during water-stress in C<sub>3</sub> plants, *Physiol. Plantarum*, 114, 231–240, 2002.
- Fournier, A., Daumard, F., Champagne, S., Ounis, A., Goulas, Y., and Moya, I.: Effect of canopy structure on sun-induced chlorophyll fluorescence, *ISPRS J. Photogramm.*, 68, 112–120, doi:10.1016/j.isprsjprs.2012.01.003, 2012.
- Frankenberg, C., Butz, A., and Toon, G. C.: Disentangling chlorophyll fluorescence from atmospheric scattering effects in O<sub>2</sub> A-band spectra of reflected sun-light, *Geophys. Res. Lett.*, 38, L03801, doi:10.1029/2010GL045896, 2011a.
- Frankenberg, C., Fisher, J. B., Worden, J., Badgley, G., Saatchi, S. S., Lee, J.-E., Toon, G. C., Butz, A., Jung, M., Kuze, A., and Yokota, T.: New global observations of the terrestrial carbon cycle from GOSAT: patterns of plant fluorescence with gross primary productivity, *Geophys. Res. Lett.*, 38, L17706, doi:10.1029/2011GL048738, 2011b.
- Frankenberg, C., O'Dell, C., Guanter, L., and McDuffie, J.: Remote sensing of near-infrared chlorophyll fluorescence from space in scattering atmospheres: implications for its retrieval and interferences with atmospheric CO<sub>2</sub> retrievals, *Atmos. Meas. Tech.*, 5, 2081–2094, doi:10.5194/amt-5-2081-2012, 2012.
- Gamon, J. A. and Berry, J. A.: Facultative and constitutive pigment effects on the Photochemical Reflectance Index (PRI) in sun and shade conifer needles Israel, *J. Plant Sci.*, 60, 85–95, doi:10.1560/IJPS.60.1-2.85, 2012.
- Gamon, J. A., Penuelas, J., and Field, C. B.: A narrow-waveband spectral index that tracks diurnal changes in photosynthetic efficiency, *Remote Sens. Environ.*, 41, 35–44, 1992.
- Guanter, L., Alonso, L., Gómez-Chova, L., Amorós-López, J., Vila-Francés, J., and Moreno, J.: Estimation of solar-induced vegetation fluorescence from space measurements, *Geophys. Res. Lett.*, 34, L08401, doi:10.1029/2007GL029289, 2007.
- Guanter, L., Alonso, L., Gómez-Chova, L., Meroni, M., Preusker, R., Fischer, J., and Moreno, J.: Developments for vegetation fluorescence retrieval from spaceborne high-resolution spectrometry in the O<sub>2</sub> A and O<sub>2</sub>-B absorption bands, *J. Geophys. Res.*, 115, D19303, doi:10.1029/2009JD013716, 2010.
- Guanter, L., Frankenberg, C., Dudhia, A., Lewis, P. E., Gómez-Dans, J., Kuze, A., Suto, H., and Grainger, R. G.: Retrieval and global assessment of terrestrial chlorophyll fluorescence from GOSAT space measurements, *Remote Sens. Environ.*, 121, 236–251, 2012.
- Guanter, L., Rossini, M., Colombo, R., Meroni, M., Frankenberg, C., Lee, J.-E., and Joiner, J.: Using field spectroscopy to assess the potential of statistical approaches for the retrieval of sun-induced chlorophyll fluorescence from space, *Remote Sens. Environ.*, 133, 52–61, 2013.
- Jacquemoud, S., Verhoef, W., Baret, F., Bacour, C., Zarco-Tejada, P. J., Asner, G. P., Francois, C., and Ustin, S. L.: PROSPECT + SAIL models: a review of use for vegetation characterization, *Remote Sens. Environ.*, 113, S56–S66, 2009.
- Joiner, J., Yoshida, Y., Vasilkov, A. P., Yoshida, Y., Corp, L. A., and Middleton, E. M.: First observations of global and seasonal terrestrial chlorophyll fluorescence from space, *Biogeosciences*, 8, 637–651, doi:10.5194/bg-8-637-2011, 2011.
- Joiner, J., Yoshida, Y., Vasilkov, A. P., Middleton, E. M., Campbell, P. K. E., Yoshida, Y., Kuze, A., and Corp, L. A.: Filling-in of near-infrared solar lines by terrestrial fluorescence and other geophysical effects: simulations and space-based observations from SCIAMACHY and GOSAT, *Atmos. Meas. Tech.*, 5, 809–829, doi:10.5194/amt-5-809-2012, 2012.
- Lichtenthaler, H. K.: Chlorophyll fluorescence signatures of leaves during the autumnal chlorophyll breakdown, *J. Plant Physiol.*, 131, 101–110, 1987.
- Louis, J., Ounis, A., Ducruet, J.-M., Evain, S., Laurila, T., Thum, T., Aurela, M., Wingsle, G., Alonso, L., Pedros, R., and Moya, I.: Remote sensing of sunlight-induced chlorophyll fluorescence and reflectance of Scots pine in the boreal forest during spring recovery, *Remote Sens. Environ.*, 96, 37–48, 2005.
- Lucht, W., Schaaf, C. B., and Strahler, A. H.: An algorithm for the retrieval of albedo from space using semiempirical BRDF models, *IEEE T. Geosci. Remote.*, 38, 977–998, 2000.
- Marquardt, D. W.: An algorithm for least-squares estimation of non-linear parameters, *J. Soc. Ind. Appl. Math.*, 11, 431–441, 1963.
- Mazzoni, M., Falorni, P., and Del Bianco, S.: Sun-induced leaf fluorescence retrieval in the O<sub>2</sub>-B atmospheric absorption band, *Opt. Express*, 10, 7014–7022, 2008.
- Mazzoni, M., Falorni, P., and Verhoef, W.: High-resolution methods for fluorescence retrieval from space, *Opt. Express*, 15, 15649–15663, 2010.

- Mazzoni, M., Meroni, M., Fortunato, C., Colombo, R., and Verhoef, W.: Retrieval of maize canopy fluorescence and reflectance by spectral fitting in the O<sub>2</sub>-A absorption band, *Remote Sens. Environ.*, 124, 72–82, 2012.
- Meroni, M. and Colombo, R.: Leaf level detection of solar induced chlorophyll fluorescence by means of a subnanometer resolution spectroradiometer, *Remote Sens. Environ.*, 103, 438–448, 2006.
- Meroni, M., Picchi, V., Rossini, M., Cogliati, S., Panigada, C., Nali, C., Lorenzini, G., and Colombo, R.: Leaf level early assessment of ozone injuries by passive fluorescence and photochemical reflectance index, *Int. J. Remote Sens.*, 29, 5409–5422, 2008.
- Meroni, M., Rossini, M., Guanter, L., Alonso, L., Rascher, U., Colombo, R., and Moreno, J.: Remote sensing of solar-induced chlorophyll fluorescence: review of methods and applications, *Remote Sens. Environ.*, 113, 2037–2051, 2009.
- Meroni, M., Busetto, L., Colombo, R., Guanter, L., Moreno, J., and Verhoef, W.: Performance of spectral fitting methods for vegetation fluorescence quantification, *Remote Sens. Env.*, 114, 363–374, 2010.
- Middleton, E. M., Corp, L. A., and Campbell, P. K. E.: Comparison of measurements and FluorMOD simulations for solar induced chlorophyll fluorescence and reflectance of a corn crop under nitrogen treatments, *Intl. J. Rem. Sensing, Special Issue for the Second International Symposium on Recent Advances in Quantitative Remote Sensing (RAQRSII)*, 29, 5193–5213, 2008.
- Middleton, E. M., Cheng, Y.-B., Corp, L. A., Huemmrich, K. F., Campbell, P. K. E., Zhang, Q.-Y., Kustas, W. P., and Russ, A. L.: Diurnal and seasonal dynamics of canopy-level solar-induced chlorophyll fluorescence and spectral reflectance indices in a cornfield, in: *Proc. 6th EARSeL SIG Workshop on Imaging Spectroscopy*, Tel-Aviv, Israel, 16–19 March, CD-Rom, 12 pp., 2009.
- Miller, J. R., Berger, M., Goulas, Y., Jacquemoud, S., Louis, J., Moise, N., Mohammed, G., Moreno, J., Moya, I., Pedrós, R., Verhoef, W., and Zarco-Tejada, P. J.: Development of a Vegetation Fluorescence Canopy Model, ESTEC Contract No. 16365/02/NL/FF, Final Report, 2005.
- Munro, R., Eisinger, M., Anderson, C., Callies, J., Corpaccioli, E., Lang, R., Lefebvre, A., Livschitz, Y., and Perez Albinana, A.: GOME-2 on MetOp: from In-Orbit Verification to Routine Operations, in: *Proceedings of EUMETSAT Meteorological Satellite Conference*, Helsinki, Finland, 12–16 June 2006.
- O'Dell, C. W., Connor, B., Bösch, H., O'Brien, D., Frankenberg, C., Castano, R., Christi, M., Eldering, D., Fisher, B., Gunson, M., McDuffie, J., Miller, C. E., Natraj, V., Oyafuso, F., Polonsky, I., Smyth, M., Taylor, T., Toon, G. C., Wennberg, P. O., and Wunch, D.: The ACOS CO<sub>2</sub> retrieval algorithm – Part 1: Description and validation against synthetic observations, *Atmos. Meas. Tech.*, 5, 99–121, doi:10.5194/amt-5-99-2012, 2012.
- Pedrós, R., Goulas, Y., Jacquemoud, S., Louis, J., and Moya, I.: FluorMODleaf: a new leaf fluorescence emission model based on the PROSPECT model, *Remote Sens. Environ.*, 114, 155–167, 2010.
- Plascyk, J. A. and Gabriel, F. C.: The Fraunhofer Line Discriminator MKII – an airborne instrument for precise and standardized ecological luminescence measurement, *IEEE T. Instrum. Meas.*, 24, 306–313, 1975.
- Preusker, R. and Lindstrot, R.: Remote sensing of cloud-top pressure using moderately resolved measurements within the oxygen A band – a sensitivity study, *J. Appl. Meteorol. Clim.*, 48, 1562–1574, 2009.
- Rascher, U.: FLEX – Fluorescence EXplorer: a remote sensing approach to quantify spatio-temporal variations of photosynthetic efficiency from space, *Photosynth. Res.*, 91, 293–294, 2007.
- Rascher, U., Agati, G., Alonso, L., Cecchi, G., Champagne, S., Colombo, R., Damm, A., Daumard, F., de Miguel, E., Fernandez, G., Franch, B., Franke, J., Gerbig, C., Gioli, B., Gómez, J. A., Goulas, Y., Guanter, L., Gutiérrez-de-la-Cámara, Ó., Hamdi, K., Hostert, P., Jiménez, M., Kosvancova, M., Lognoli, D., Meroni, M., Miglietta, F., Moersch, A., Moreno, J., Moya, I., Neininger, B., Okujeni, A., Ounis, A., Palombi, L., Raimondi, V., Schickling, A., Sobrino, J. A., Stellmes, M., Toci, G., Toscano, P., Udelhoven, T., van der Linden, S., and Zaldei, A.: CEFLES2: the remote sensing component to quantify photosynthetic efficiency from the leaf to the region by measuring sun-induced fluorescence in the oxygen absorption bands, *Biogeosciences*, 6, 1181–1198, doi:10.5194/bg-6-1181-2009, 2009.
- Rothman, L. S., Gordon, I. E., Barbe, A., Benner, D. C., Bernath, P. F., Birk, M., Boudon, V., Brown, L. R., Campargue, A., Champion, J., Chance, K., Coudert, L. H., Dana, V., Devi, V. M., Fally, S., Flaud, J. M., Gamache, R. R., Goldman, A., Jacquemart, D., Kleiner, I., Lacombe, N., Lafferty, W. J., Mandin, J., Massie, S. T., Mikhailenko, S. N., Miller, C. E., Moazzen-Ahmadi, N., Naumenko, O. V., Nikitin, A. V., Orphal, J., Perevalov, V. I., Perrin, A., Predoi-Cross, A., Rinsland, C. P., Rotger, M., Simecková, M., Smith, M. A. H., Sung, K., Tashkun, S. A., Tennyson, J., Toth, R. A., Vandaele, A. C., and Vander Auwera, J.: The HITRAN 2008 molecular spectroscopic database, *J. Quant. Spectrosc. Ra.*, 110, 533–572, 2009.
- Saito, Y., Kanoh, M., Hatake, K., Kawahara, T. D., and Nomura, A.: Investigation of laser-induced fluorescence of several natural leaves for application to lidar vegetation monitoring, *Appl. Optics*, 37, 431–437, 1998.
- Sanders, A. F. J. and de Haan, J. F.: Retrieval of aerosol parameters from the oxygen A band in the presence of chlorophyll fluorescence, *Atmos. Meas. Tech. Discuss.*, 6, 3181–3213, doi:10.5194/amt-d-6-3181-2013, 2013.
- Subhash, N. and Mohanan, C. N.: Curve-fit analysis of chlorophyll fluorescence spectra: application to nutrient stress detection in sunflower, *Remote Sens. Environ.*, 60, 347–356, 1997.
- van der Tol, C., Verhoef, W., and Rosema, A.: A model for chlorophyll fluorescence and photosynthesis at leaf scale, *Agr. Forest Meteorol.*, 149, 96–105, 2009.
- Vasilkov, A., Joiner, J., and Spurr, R.: Note on rotational-Raman scattering in the O<sub>2</sub> A- and B-bands, *Atmos. Meas. Tech.*, 6, 981–990, doi:10.5194/amt-6-981-2013, 2013.
- Veefkind, J. P., Aben, I., McMullan, K., Forster, H., de Vries, J., Otter, G., Claas, J., Eskes, H. J., de Haan, J. F., Kleipool, Q., van Weele, M., Hasekamp, O., Hoogeveen, R., Landgraf, J., Snel, R., Tol, P., Ingmann, P., Voors, R., Kruijzinga, B., Vink, R., Visser, H., and Levelt, P. F.: TROPOMI on the ESA Sentinel-5 Precursor: a GMES mission for global observations of the atmospheric composition for climate, air quality and

- ozone layer applications, *Remote Sens. Environ.*, 120, 70–83, doi:10.1016/j.rse.2011.09.027, 2012.
- Zarco-Tejada, P. J., Miller, J. R., Mohammed, G. H., and Noland, T. L.: Chlorophyll fluorescence effects on vegetation apparent reflectance: I. Leaf-level measurements and model simulations, *Remote Sens. Environ.*, 74, 582–595, 2000.
- Zarco-Tejada, P. J., Berni, J. A. J., Suarez, L., Sepulcre-Cantó, G., Morales, F., and Miller, J. R.: Imaging chlorophyll fluorescence with an airborne narrow-band multispectral camera for vegetation stress detection, *Remote Sens. Environ.*, 113, 1262–1275, 2009.
- Zarco-Tejada, P. J., Morales, A., Testi, L., and Villalobos, F. J.: Spatio-temporal patterns of chlorophyll fluorescence and physiological and structural indices acquired from hyperspectral imagery as compared with carbon fluxes measured with eddy covariance, *Remote Sens. Environ.*, 133, 102–115, 2013.